

Table of Contents

1. Introduction	1
1.1 Microsatellite.....	1
1.2 Required performance.....	3
1.3 The Thruster for Microsatellites	5
1.4 Purpose	7
2. Miniature Microwave Discharge Plasma Thruster	8
2.1 Mechanism of ion acceleration.....	8
2.2 Selection of the Propellant.....	9
2.3 Expectation of the Performance.....	10
2.4 Microwave Discharge.....	11
2.5 Magnetic Tube.....	12
3. Experimental Facility and Setup	14
3.1 Vacuum Chamber	14
3.1.1 Small Vacuum Chamber.....	14
3.1.2 Large Vacuum Chamber.....	15
3.1.3 Space Science Chamber.....	15
3.2 Miniature Microwave Discharge Thruster.....	17
3.3 Probe Measurement.....	20
3.3.1 Langmuir probe.....	20
3.3.2 Emissive probe.....	22
3.4 Retarding Potential Analyzer.....	24
3.5 Ion beam measurement.....	26
3.6 Thrust measurement.....	27
3.6.1 Hanging Pendulum Thrust Stand.....	27
3.6.2 Aluminum Target Thrust Stand.....	27
4. Experimental Result and Discussion	29
4.1 Ion Energy Measurement.....	29
4.2 Plasma Diagnostics by Langmuir Probe.....	30
4.3 Space Potential Measurement by Emissive Probe.....	33
4.4 Thrust Performance Estimation.....	36
4.5 Thrust Measurement.....	39
4.5.1 Measurement by Hanging Pendulum Thrust Stand.....	39
4.5.2 Measurement by Aluminum Target Thrust Stand.....	41

5. Summary	45
List of References	45
Acknowledgement	48

Chapter 1

Introduction

1.1 Microsatellite

Nowadays, space utilization is entwined with human life in many aspects; communication, weather forecast and car navigation system. On space utilization, microsatellite is attractive. Microsatellites account for an increasing share of satellite launches; 90% of the satellites launched in 2013 were in the 50 kg or less class. The Fig. 1-1 shows the number of launch of the 50 kg or less class satellites in 2004 ~ 2013.¹⁾ Thanks to their relatively low cost and short development time, and the possibility of the launching piggyback on other payloads,^{2,3)} microsatellites enable space access more achievable for academic teams, small companies, and developing countries.^{4,5)}

Though the capabilities of microsatellites are restricted compared with large satellites, microsatellites can be competitive with the large satellites if they adopt formation flight and constellation operation.^{6,7)} In these configurations, the damage of a trouble can be reduced and the addition of extra function is relatively easy.

Most microsatellites, however, have no thruster, since there is little room for the thrust systems and a small solar array will not allow the large power consumption of a thruster. Some challenging microsatellites, however, have a thruster like the “Hodoyoshi-3&4” and “PRoximate Object Close flyby with Optical Navigation (PROCYON)” in these days,^{8,9)} because thrusters enable advanced functionality, including the possibility of orbit transfer or orbit keeping, or even super low altitude keeping. Super low altitude satellites flight at about 180~250 km enable high resolution observation and reduce the emission power requirements for active sensors.^{10,11)} In addition, the observation device can be miniaturized, if super low altitude satellite realizes the resolution same to the one of the big satellite in high altitude. Hence, super low altitude satellite can be miniaturized. However, micro super low altitude satellite has not been developed. An obstruction of the miniaturization is propulsion system. Satellites performing these missions must, however, compensate for drags by using thrusters. Therefore, the goal of this study is development of the thruster adoptable to the micro super low altitude satellite.

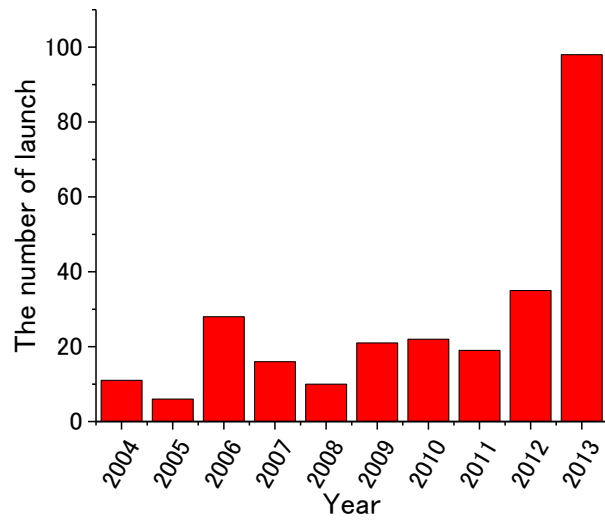


Fig. 1-1 The number of launch of the 50 kg or less class satellites in these days

1.2 Required performance

Firstly, we assumed the satellite and the mission as shown in Fig. 1-2 and Table. 1-1, respectively. Generated power is estimated by the assumption that the area of the solar panel is 0.4 m×0.5 m and the conversion efficiency of the solar panel is 40%. Secondly, we estimate the magnitude of the drag. The drag is calculated by following equation.

$$F = \frac{1}{2} \rho v^2 C_d S \quad (1-1)$$

In this equation, ρ , v , C_d and S represent the density of the air, the velocity of the satellite, drag coefficient and the area of the projected area against the direction of movement. These parameters are assumed that ρ is $3.5 \times 10^{-9} \text{ kg/m}^3$ and v is the velocity of the satellite at the altitude of 200 km (7.8 km/s). C_d is changeable by the parameter of the atmosphere and shape of the satellites. In the case of Super Low Altitude Test Satellite (SLATS), C_d is 0.2~1 when the attack angle is 0~30 deg.¹²⁾ If this parameter is adopted, the drag is estimated to be 0.2~1 mN. Therefore, we set the objective thrust as 1 mN. The power used for thrust system should be 20~30% for widely application, so the objective power consumption of the thruster system is under 20 W. Specific impulse is also important parameters for thruster system. Specific impulse is defined in the following equation and it represent the duration of the unit thrust by using unit propellant mass.¹⁵⁾

$$I_{sp} = \frac{F}{\dot{m}g} \cong \frac{v_i}{g} \quad (1-1)$$

In this equation, F , \dot{m} and g represent the thrust and mass flow rate and gravitational acceleration. The nearly equal is valid only when 100% of the propellant gas is utilized. The unit of specific impulse (I_{sp}) is s. Optimum specific impulse is estimated from following equation.¹³⁾

$$(I_{sp})_{opt} = \frac{\sqrt{\alpha\tau}}{g} \quad (1-2)$$

In this equation, α is the ratio of the thrust power and thruster system weight, and the unit is W/kg. The weight of the thruster system is assumed to be 5 kg in reference to the miniature ion engine system for microsatellite.¹⁴⁾ From these assumption, α and τ is calculated as following.

$$\alpha = \frac{1[mN] \times 7.8[km/s]}{5[kg]} = 1.56[W/kg] \quad (1-3)$$

τ is the operational time of the thruster and the unit is s. τ is calculated as 6.31×10^7 sec

from mission period. From these parameters, the optimum specific impulse is estimated as 1000 sec. From the above, the required performance is are 1 mN and 1000 sec, respectively, with a total power consumption of 20 W in the thruster system. In addition, the simplicity of the thrust system is also important. Simple structure provide the high robustness, compactness, light weight and low cost. These are very important point for microsatellite. Therefore, the objective performance should be achieved with the simple thrust system.

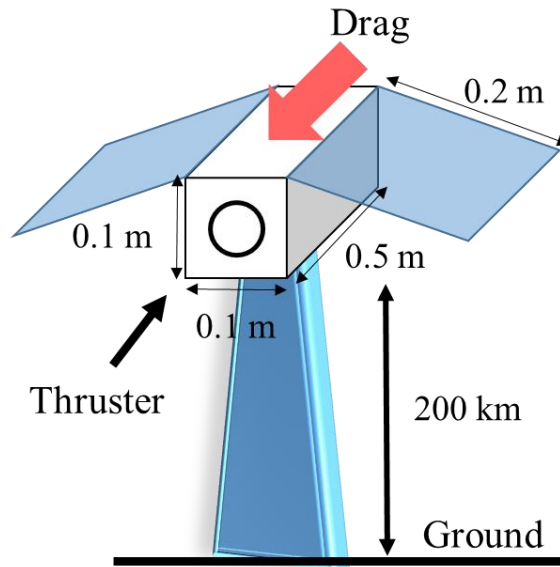


Fig. 1-2 Image of the assumed satellites

Table. 1-1 The Properties of the assumed satellite

Altitude	200 km
Size	0.1 m×0.1 m×0.5 m
Mass	50 kg
Power generation	100 W
Mission period	2 years

1.3 The Thruster for Microsatellites

There are two types in the thruster for space craft; chemical propulsion and electric propulsion. Chemical thruster gain a thrust by exhaustion of the high temperature and high pressure gas made by combustion of fuel and oxidizer. The Feature of the chemical propulsion is high thrust and low specific impulse.

Electric Propulsion use the electric energy to expel the ionized propellant. Many satellites operate with electric propulsion; there are 236 operational satellites as of 2013.¹⁶⁾ The feature of the electric propulsion is high specific impulse, so propellant mass can be saved by adoption the electric propulsion. Electric propulsion systems are suitable for the drag compensation because the thrusters should operate while keeping the orbits and the mounted propellant mass is restricted. “Gravity Field and Steady-State Ocean Circulation Explorer (GOCE)” with a mass of 1100 kg, used two 20 mN class ion thrusters.¹⁷⁾ “SLATS” will also use an ion thruster. Therefore, we also adopted electric propulsion. However, it is difficult to fulfill this thrust performance using existing electric propulsions. Some thruster for micro/nano satellites is under developing, but there is no thruster which achieved objective performance with simple structure.^{18),19)} A power consumption will be over 10 W, if 1 mN thrust is realized by a miniature ion thruster.²⁰⁾ For example, Table. 2 shows the breakdown of the power consumption is a miniature ion thruster developed in Kyushu University.²¹⁾ In this power consumption, the thrust performance is that thrust and specific impulse is 0.57 mN and 2972 sec, respectively. As shown in this table, the total power consumption is 30 W. In addition, it is also hard that the specific impulse of 1000 sec is realized by the existing thruster. Figure 1-3 shows the relationship between the thrust and specific impulse of the thruster. As shown in this Figure, there is no thruster which has the specific impulse of 1000 sec. Therefore, it is necessary that the development of a novel thruster.

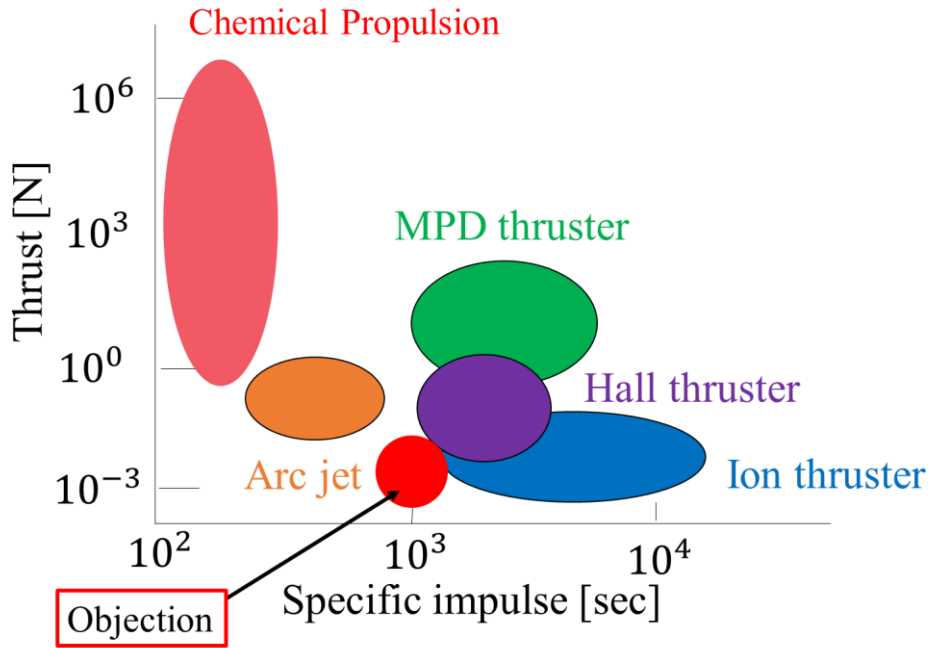


Fig. 1-3 The relationship of the thrust and the specific impulse

Table. 1-2 Breakdown of the power consumption in miniature ion thruster

Ionization in the ion thruster	8 W
Ion acceleration	12 W
Ionization in the neutralizer	2 W
Others (Conversion efficiency etc...)	8 W
Total power consumption	30 W

1.4 Purpose

Development of the thruster for the micro super low altitude satellite is our definitive purpose. Hence, we have been developing a miniature microwave discharge thruster and some parameters were optimized.²²⁾ Figure 1-4 shows the photo of the thruster. We adopted a thruster concept as shown in Chapter 2 using a microwave discharge, which doesn't have the device to accelerate ions actively. This is because the main power consumption of the ion thruster is used for ion acceleration as shown in Table. 1-2. If the ion acceleration power is saved, the power consumption of the thruster head will 10 W and total power consumption of the thrust system can be under 20 W. In addition, the power supply for the grid is also saved. However, the mechanism of ion acceleration is not shown yet and the thrust performance is not clear. Therefore, the purpose of this study is to show the ion acceleration mechanism of the thruster and evaluate the thrust performance exactly.

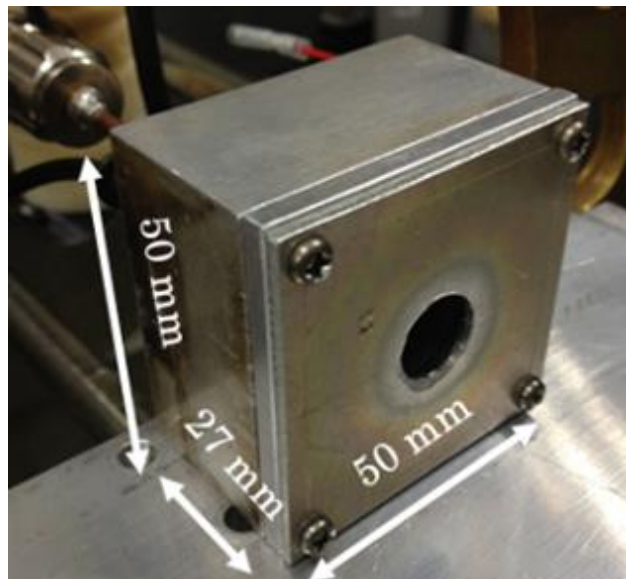


Fig. 1-4 Photo of the miniature microwave discharge thruster

Chapter 2

Miniature Microwave Discharge Plasma Thruster

2.1 Mechanism of ion acceleration

Figure 2-1 shows a schematic of the ion acceleration mechanism of this thruster. The plasma is generated by microwave discharge. Electrons are trapped by a magnetic field, in the area between magnetic mirrors. This magnetic configuration is called the magnetic tube and this configuration is used in some microwave discharge neutralizer and ion thruster head.²³⁾ Electrons gain energy from the microwaves, they collide with propellant particles, and the propellant atoms are ionized. The ions are accelerated by the potential difference between the plasma inside the thruster and the space, if the potential of the discharge chamber was kept at the space potential. High energetic electrons can also go out to downstream with ions against the potential hill. These electrons and ions are neutralized outside the thruster; it does not need a neutralizer. Therefore, this thruster is very simple and small, with low power requirements.

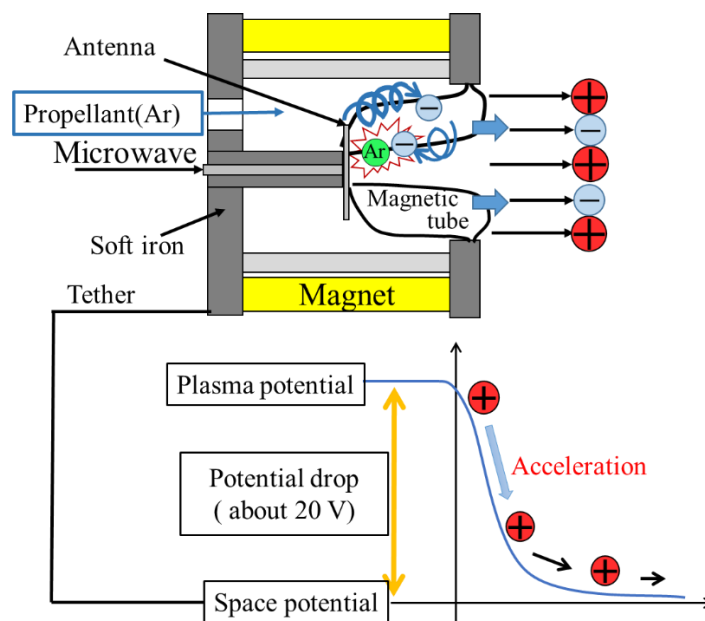


Fig. 2-1 Mechanism of ion acceleration.

2.2 Selection of the Propellant

Xenon is widely used as propellant in electric propulsion, because the ionization cost become low owing to a low ionization energy relatively in the rare gas. However, in this study, Argon is used as propellant on account of high specific impulse and low cost. Specific impulse is in inverse proportion to the mas of the propellant, so specific impulse become longer by adopting Argon. The price of Argon is about 1/1000 of the one of Xenon, because 1% of atmosphere is Argon. Table. 2-1 shows the cost and production of the Argon and Xenon.²⁴⁾ Cost is the important for widely application of thrust system in the future.

Table. 2-1 Cost and production of Xenon and Argon

	Production [t /year]	Potential production [t /year]	Unit price [JPY/kg]
Xe	32	160	500,000
Ar	3×10^6	5×10^6	500

2.3 Expectation of the Performance

It is needed to validate that the thruster concept can meet the required performance. The potential difference between the plasma inside the thruster and the space is estimated as 20 V, because the sheath potential is 20 V on the simulation of a miniature microwave discharge neutralizer in Kyushu University.²⁵⁾ In that case, the velocity of the extracted ion v_i is calculated by following equation from the ion's equation of motion.

$$v_i = \sqrt{\frac{2\varphi e}{m_i}} \quad (2-1)$$

In this equation, φ , e and m_i is represent the potential difference, elemental charge and ion mass. From this equation, the ion velocity is 9800 m/s, and the specific impulse is 1000 sec in the case of the propellant utilization of 1. Propellant utilization represent the percent of the propellant extracted as ion beam current to the mass flow rate and defined in the following equation.

$$\eta_u = \frac{I_b m_i}{e \dot{m}} \quad (2-2)$$

I_b means the ion beam current. In this case, thrust is estimated as 1 mN from following equation.

$$F = \dot{m} v = \frac{m_i}{e} I_b v_i \quad (2-3)$$

Therefore, this thruster concept can meet the objective performance.

2.4 Microwave Discharge

We adopted the microwave discharge for plasma generation. The utility of microwave discharge is shown in the mission of HAYABUSA.²⁶⁾ Microwave discharge have the merits for thruster shown in the below.

- 1) Long lifetime and simplification owing to the lack of the electrode
- 2) Needlessness of the beforehand heating
- 3) Low power consumption by using existing electron

In this thruster, Electron Cyclotron Resonance (ECR) is used to give the energy to the electron. In this thruster, however, it seemed that the electron cyclotron wave doesn't propagate because the size of the discharge chamber is much smaller than the wave length of the microwave. Electric field to accelerate electron seemed to be generated by the potential difference of the discharge chamber and antenna. ECR is occurred by the oscillation of the antenna potential at microwave frequency. In this thruster, plasma is also generated in front of the antenna.²⁷⁾ This shows that the electron can be accelerated enough without ECR.

2.5 Magnetic Tube

In this thruster, the magnetic tube is formed between the central yoke and front yoke as shown in Fig. 2-2. Electrons make a round trip between the central yoke and front yoke along the magnetic lines of force and reflected at the both ends by the sheath potential. Magnetic mirrors in the both ends also contribute the reflection of the electron. Electrons gain energy from microwave by approaching the strong electric field area near the antenna many times. Plasma can be generated effectively on account of this effect. In the magnetic tube, guiding center also do ∇B drift because the magnetic field strength is large and it generate the ∇B along the magnetic tube. Therefore, the total movement of electrons is as shown in Fig. 2-3.

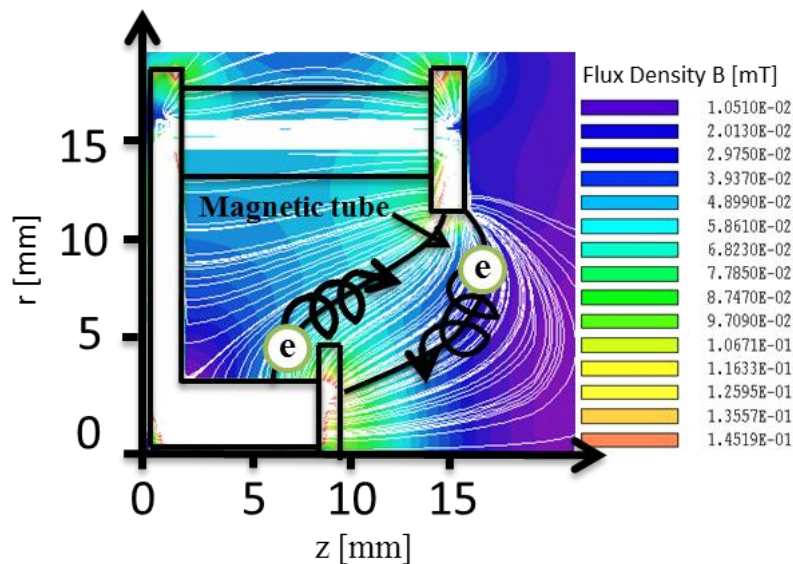


Fig. 2-2 Confinement by magnetic tube

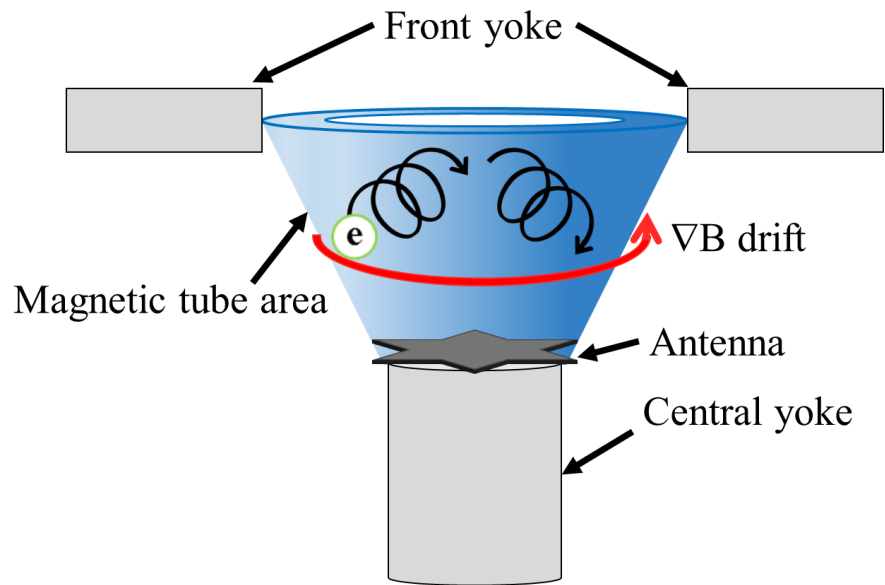


Fig. 2-3 ∇B drift in the magnetic tube

Chapter 3

Experimental Facility and Setup

3.1 Vacuum Chamber

3.1.1 Small Vacuum Chamber

Experiments was conducted in the three types of the vacuum chamber. Fig. 3-1 shows the small vacuum chamber in Kyushu University. The inner diameter and the length of the vacuum chamber are 0.6 m and 1.0 m, respectively. The pumping system consists of a rotary pump (pumping speed $1.5 \times 10^{-2} \text{ m}^3/\text{sec}$) and turbo molecular pumps (pumping speed $5.2 \times 10^{-1} \text{ m}^3/\text{sec}$). The chamber baseline pressure is below $5.7 \times 10^{-4} \text{ Pa}$. The back pressure is $2.7 \times 10^{-2} \text{ Pa}$ at the argon mass flow rate of $82 \text{ } \mu\text{g}/\text{sec}$. This vacuum chamber is connected to GND through whole experiments and this is the baseline voltage.



Fig. 3-1 Small vacuum chamber

3.1.2 Large Vacuum Chamber

Fig. 3-2 shows the large vacuum chamber in Kyushu University. The inner diameter and the length of the vacuum chamber are 1.0 m and 1.2 m, respectively. The pumping system consists of a rotary pump (pumping speed $2.7 \times 10^{-2} \text{ m}^3/\text{sec}$), mechanical booster pump ($1.0 \times 10^{-1} \text{ m}^3/\text{sec}$) and turbo molecular pumps (pumping speed $2.2 \text{ m}^3/\text{sec}$). The chamber baseline pressure is below $1.7 \times 10^{-3} \text{ Pa}$. The back pressure is $3.6 \times 10^{-3} \text{ Pa}$ at the argon mass flow rate of $82 \text{ } \mu\text{g}/\text{sec}$. This vacuum chamber is connected to GND through whole experiments and this is the baseline voltage.

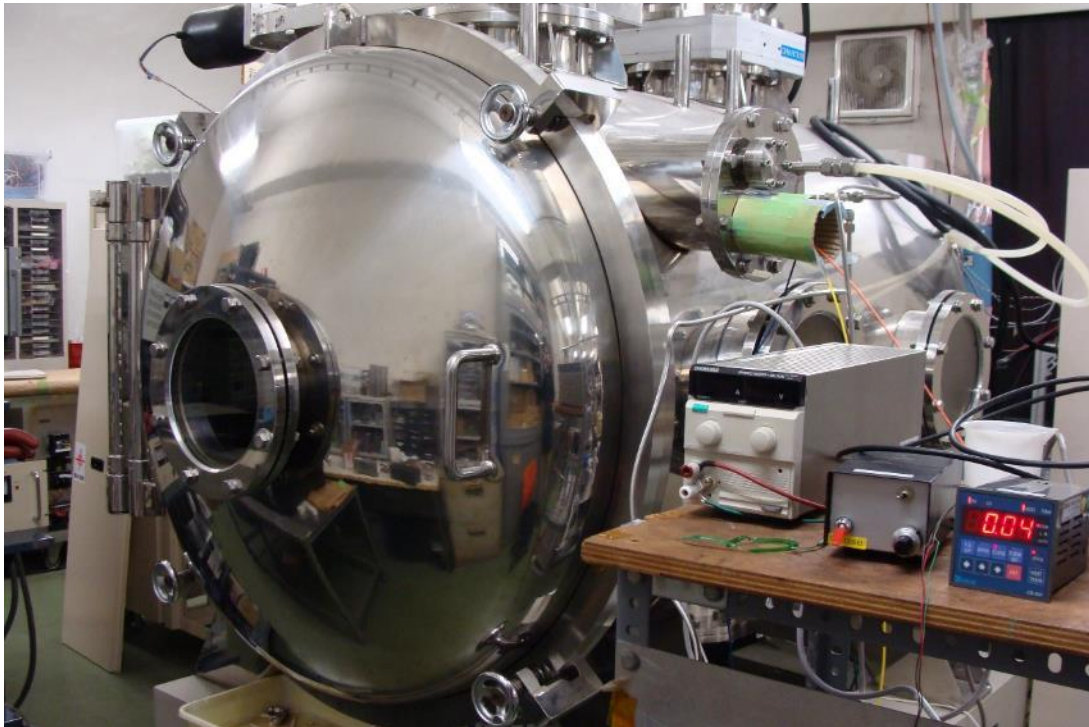


Fig. 3-2 Large vacuum chamber

3.1.3 Space Science Chamber

Fig. 3-3 shows the Space Science Chamber at the Institute of Space and Astronautical Science (ISAS) of Japan Aerospace Exploration Agency. The diameter and the length of the vacuum chamber are 2.5 m and 5.0 m, respectively. The pumping system consists of a turbo molecular pump (pumping speed $3.4 \times 10^3 \text{ l/s}$ at N_2) and two cryo pumps (pumping speed $2.8 \times 10^4 \text{ l/s}$ at N_2). The chamber baseline pressure is below $2.28 \times 10^{-4} \text{ Pa}$. The back pressure is $3.28 \times 10^{-4} \text{ Pa}$ at an argon mass flow rate of $84 \text{ } \mu\text{g}/\text{sec}$. The back pressure is $1.69 \times 10^{-2} \text{ Pa}$ with the back ground plasma. The back ground argon plasma is generated by backward diffusion type plasma generator and the density is $7 \times 10^{11} - 1 \times 10^{12} \text{ m}^{-3}$. The

discharge current is 100-200 mA and the pressure is 0.02 Pa. Fig. 3-4 shows the photo of the plasma generator.



Fig. 3-3 Space science chamber at ISAS

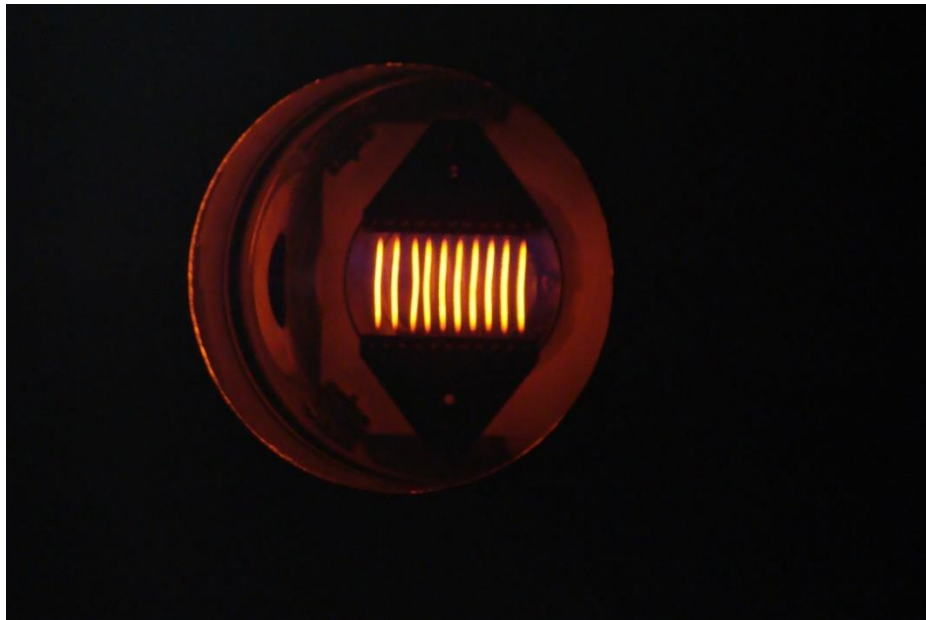


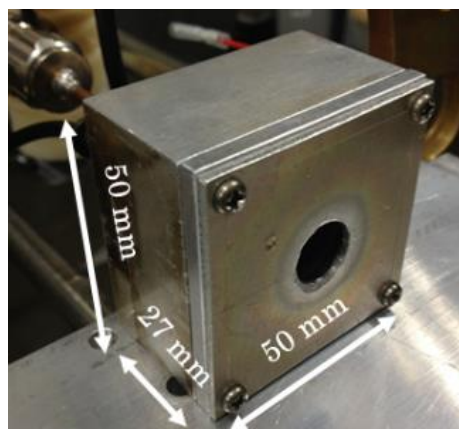
Fig. 3-4 Photo of the plasma generator

3.2 Miniature Microwave Discharge Thruster

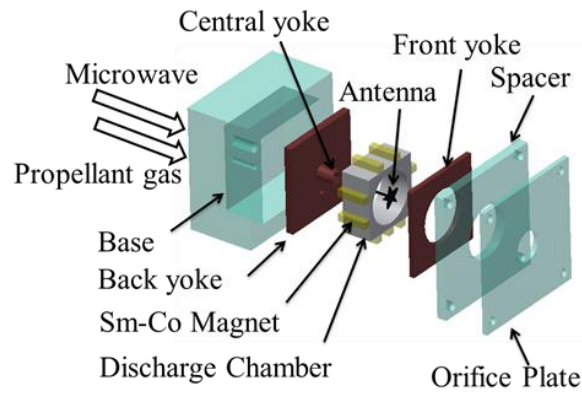
In this study, the two types of the thruster is developed. Figures 3-5 (a) and (c) show the two microwave discharge thrusters; one is 50 mm×50 mm×27 mm and the other is 50 mm×50 mm×53.5 mm. Fig. 3-5(b) shows the parts assembly of the thruster with 12 mm discharge chamber length. Sm-Co magnets surround the discharge chamber and are located between yokes made of soft iron. The magnet size is 4 mm×4 mm×12 mm. The inner diameter of the discharge chamber is 21 mm and its height is 12 mm. There are a spacer (diameter 36 mm) and an orifice plate (diameter 12 mm) in front of the front yoke. The thickness of the spacer and orifice are 4 mm and 2 mm respectively. The antenna is made of molybdenum. The antenna, which is star shaped, has a thickness of 1 mm and a circular diameter of 9 mm. This star shaped antenna showed best performance in the previous study.²⁹⁾

Figure 3-5 (d) shows the parts assembly of the thruster with 33 mm discharge chamber length. The discharge chamber is extended to 33 mm. The magnets and the central yoke are extended to fit the discharge chamber. The back yoke is enlarged from 35 mm×35 mm×3 mm to 50 mm×50 mm×12 mm. The other yokes are the same dimensions as of the 12 mm discharge chamber thruster.

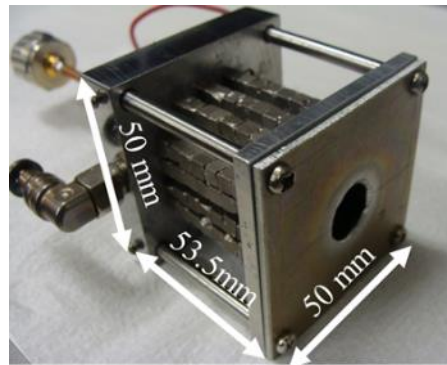
The magnetic field strength inside the discharge chamber can be changed by changing the number of magnets. Figure 3-6 shows the magnetic field distribution for 9 magnets (12 mm discharge chamber) and 14 magnets (33 mm discharge chamber). The number of magnets is optimized for the best performance, the detail was shown in Ref. 30.



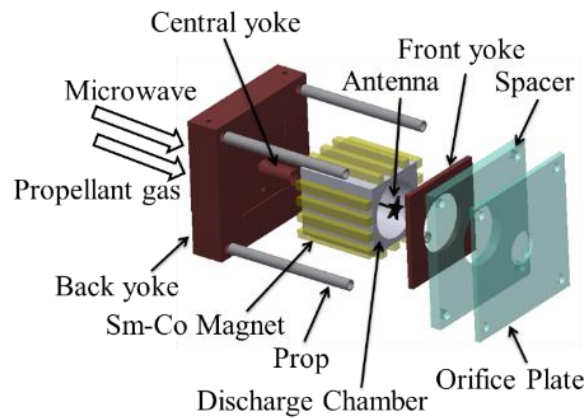
(a)



(b)

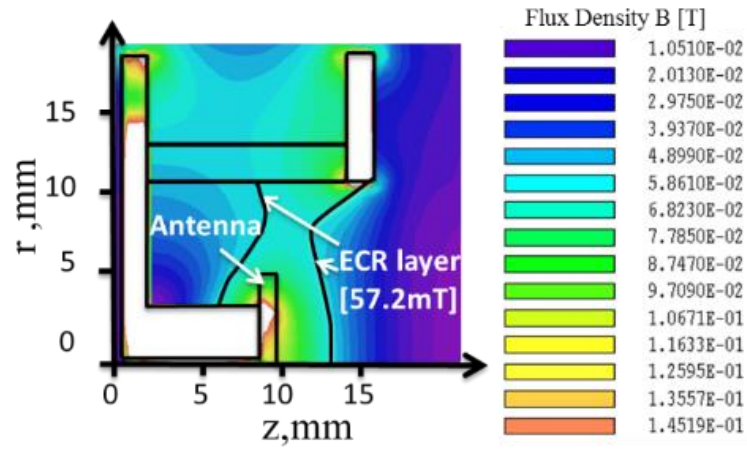


(c)

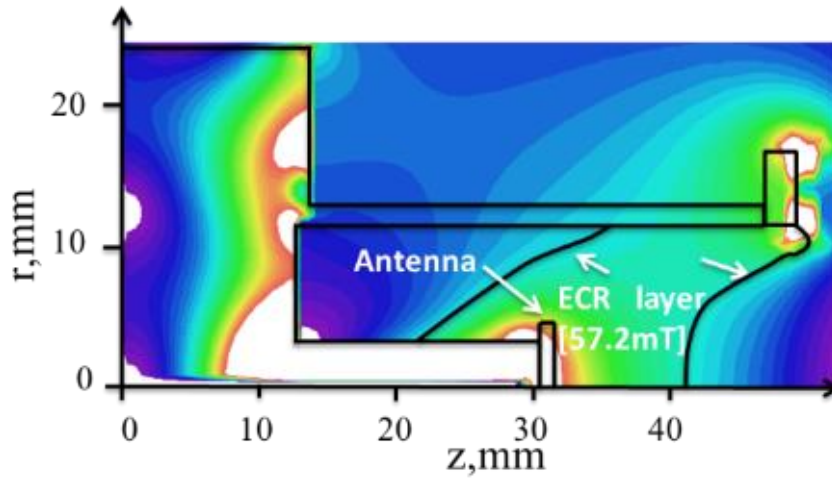


(d)

Fig. 3-5. Microwave discharge thrusters (a) photo of 12 mm discharge chamber type, (b) parts assembly of 12 mm discharge chamber type, (c) photo of 33 mm discharge chamber type, (d) parts assembly of 33 mm discharge chamber type.



(a)



(b)

Fig. 3-6. Magnetic field distribution for each discharge chamber (a) 12 mm discharge chamber type and (b) 33 mm discharge chamber type.

3.3 Probe Measurement³¹⁾

3.3.1 Langmuir probe

Ion acceleration mechanism can be investigated by probe measurement. In this study, two types of the probe is used; Langmuir probe and emissive probe. Figure 3-7 shows the photo of the Langmuir probe used in this study. The Langmuir probe is installed in the linear actuator and inserted to the thruster from the downstream on the center axis of the thruster as shown in Fig. 3-8.

In Langmuir probe measurement, plasma parameter is gained following procedure. The I-V characteristic as shown in Fig. 3-9 is gained by the probe measurement. The horizontal axis V_p shows the probe voltage and the horizontal axis I_p shows the current flowing into the probe. The positive direction of the vertical axis corresponds to the electron current flows into the probe. I_{es} , I_{is} , V_f and V_s , shows the electron saturation current, ion saturation current, floating potential and plasma potential, respectively. This V-I characteristic divided three regions. First region is the right region and this region is ion saturation current region. In this region, the probe voltage is much lower than the plasma potential and electrons are reflected by potential difference and only ion flows through probe. Second region is retarding potential region and it is a middle region of the figure. In this region, probe current increases with the increase of the probe voltage. This is because electrons begin to flow into the probe. Third region is an electron saturation region. In this region, all ion is reflected and only electrons flow into the probe. Plasma parameters can be founded as following.

1) Electron temperature T_e

In the retarding potential region, the following equation can be obtained.

$$\frac{d \ln I_e(V_p)}{dV} = -\frac{e}{T_e} \quad (3-1)$$

As shown in this equation, electron temperature can be obtained from the slope in the I-V characteristic plotted in the semilog graph. Note that I_e is not equal to the I_p , so I_e is obtained by subtracting I_i form I_p . I_i in the retarding potential region can be obtained by extrapolation as shown (a) in Fig. 3-9.

2) Plasma potential

Plasma potential V_s is obtained as the voltage of the cross point of the tangent lines in the retarding potential region and electron saturation current region on the semilog graph.

3) Electron density

Electron density is obtained by electron saturation current or ion saturation current. In this study, electron saturation current is decreased by magnetic field, so electron density is obtained from ion saturation current. Electron density is obtained from following equation.

$$I_{is} = n_e e S \left(\frac{k_b T_e}{m_i} \right)^{1/2} \exp\left(-\frac{1}{2}\right) \quad (3-2)$$



Fig. 3-7 Photo of the Langmuir Probe

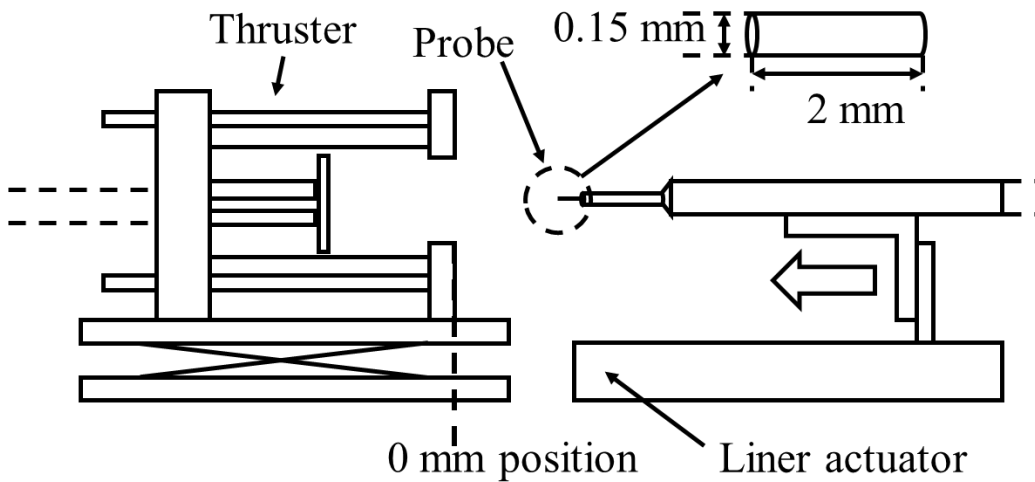


Fig. 3-8 Schematics of the probe measurement

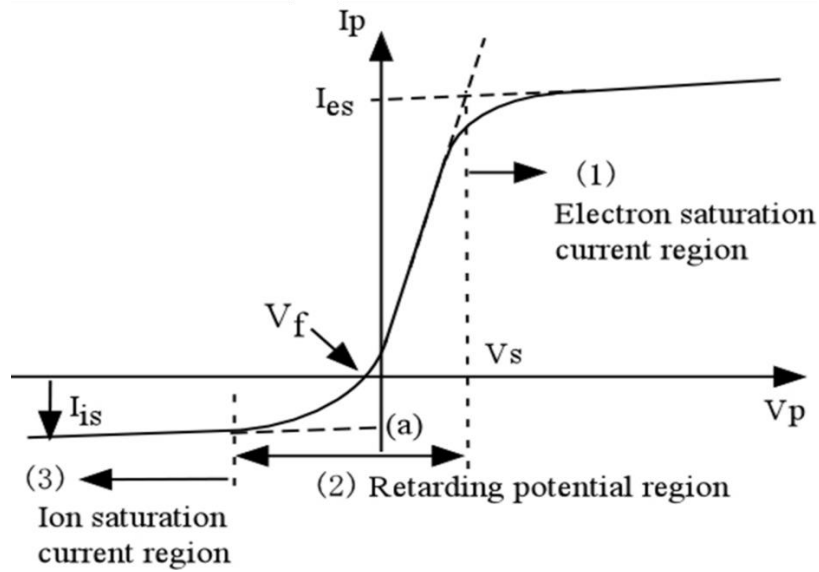


Fig. 3-9 I-V characteristic gained by Langmuir probe

3.3.2 Emissive probe

Emissive probe is used for potential measurement. Emissive probe can measure the space potential more exactly than the Langmuir probe. Figure 3-10 shows the I-V characteristic gained by emissive probe. Emissive probe is heated and emit the electrons. Emitted electrons are accelerated by ion sheath and flow into the plasma. Ion current flow into the probe increase and the slope in the retarding potential region increase as shown in Fig. 3-10. Therefore, if the heating and electron emission is enough, the floating potential V_f can be regard as the plasma potential V_s . Therefore, we measured the floating potential of the emissive probe. Fig. 3-11 shows the missive probe used in this study. Emissive probe is made of the 1% thoriated tungsten and the diameter of the filament is 0.125 mm. The emissive probe is connected to the power supply via transformer and applied 8 kHz sine wave of 10-11 A. This sine wave prevents the potential difference in the filament.

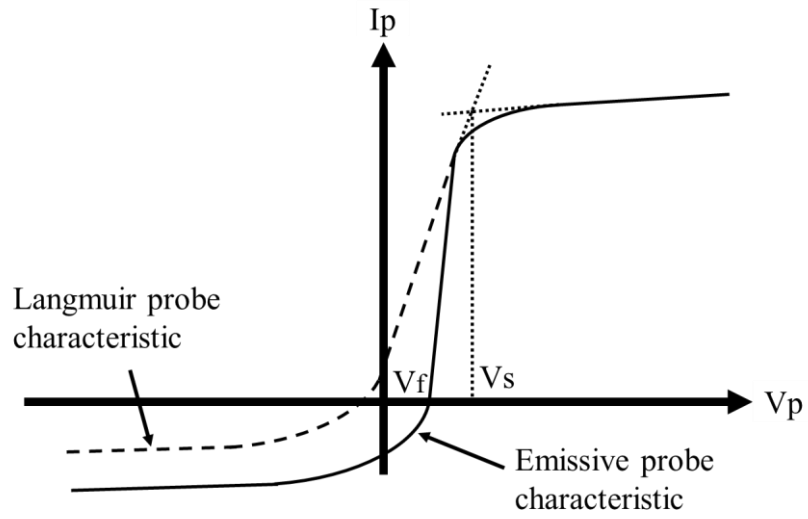


Fig. 3-10 I-V characteristic gained by emissive probe



Fig. 3-11 Photo of the emissive probe

3.4 Retarding Potential Analyzer

Retarding Potential Analyzer (RPA) is used to measure the extracted ions energy. Fig. 3-12 and Fig. 3-13 shows the photo of the RPA and the schematic of retarding potential analyzer, respectively. The RPA consists of four grids and one collector, as shown in Fig. 3-13. We measured the collector current while scanning the voltage of the Ion Retarding Grid (IRG) from 0 to 65 V. We apply -40 V to the Electron Retarding Grid (ERG) and Secondary Electron Suppression Grid (SESG). The Floating Grid (FG), ERG and SESG are 200 mesh/inch, the IRG is 400 mesh/inch. The FG is the three-ply 200 meshes. This is to prevent the ionization of the neutral particles and space charge limitation by decreasing the number of ions and neutral particles flowing into the RPA. The IRG has fine mesh to prevent generation of an area where the voltage is lower than that applied in the mesh. The following equation was used to calculate Ion Energy Distribution Function (IEDF) $f(E_i)$.³²⁾

$$f(E_i) = -\frac{1}{eI_{c0}} \frac{dI_c}{dV_{RG}} \quad (3-3)$$

In this equation, V_{RG} and I_c represent grid sweep voltage and collector current. I_{c0} represent the collector voltage when the sweep voltage is 0 V. Average of the ion energy $E_{i,ave}$ is gained from following equation.

$$E_{i,ave} = \int_0^{+\infty} E_i f(E_i) dE_i \quad (3-4)$$

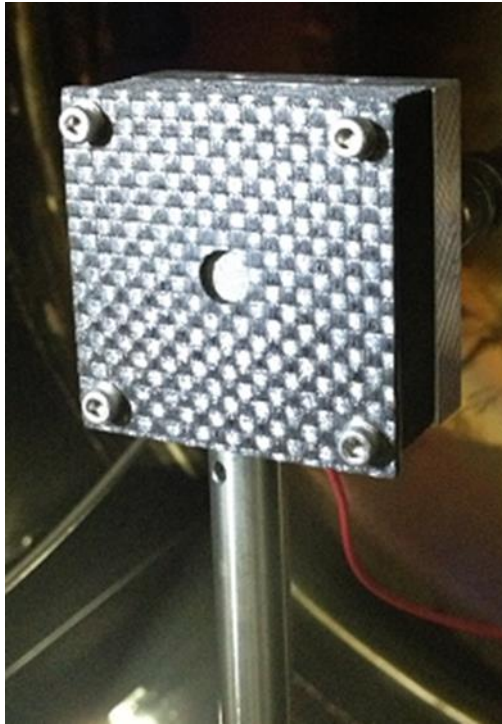


Fig. 3-12 Photo of the retarding potential analyzer

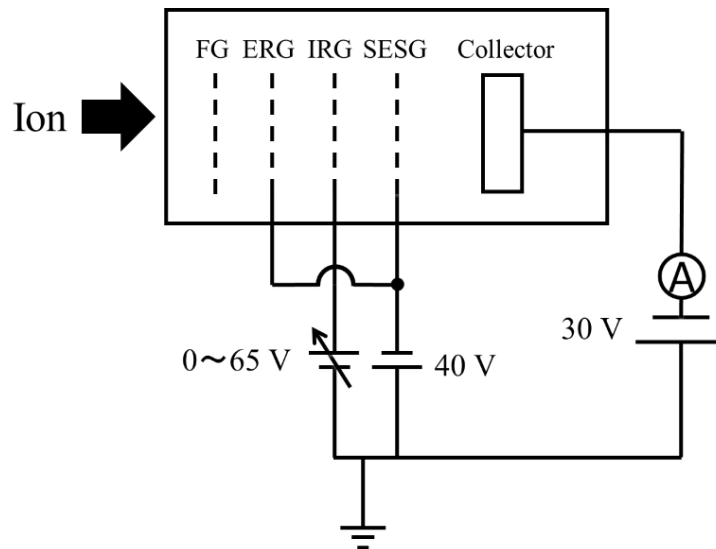


Fig. 3-13 Schematic of retarding potential analyzer

3.5 Ion beam measurement

Ion beam was measured to estimate the thrust performance. Fig. 3-14 shows the schematics of the ion beam measurement. In order to repel the electrons, -30 V is applied to the ion collector and the ion current is saturated at -30 V. Fig. 3-15 shows the ion collector used in this study. In previous study, it seemed that extracted ion is scattered by charge exchange collision.³³⁾ The cylindrical collector can collect the scattered ions. This collector is perforated, and has an aperture ratio of 48% to prevent the confinement of neutral particles.

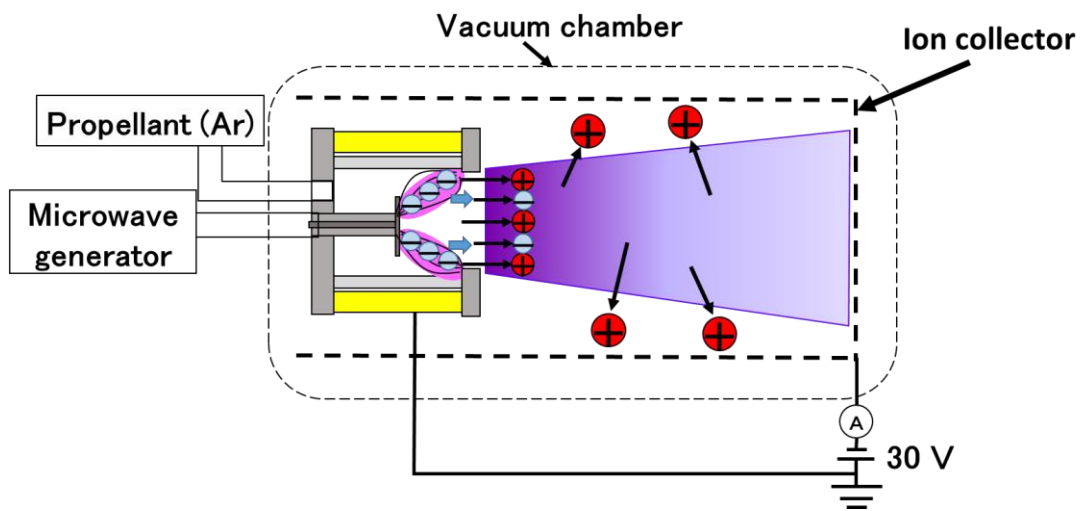


Fig.3-14 Schematics of ion beam measurement

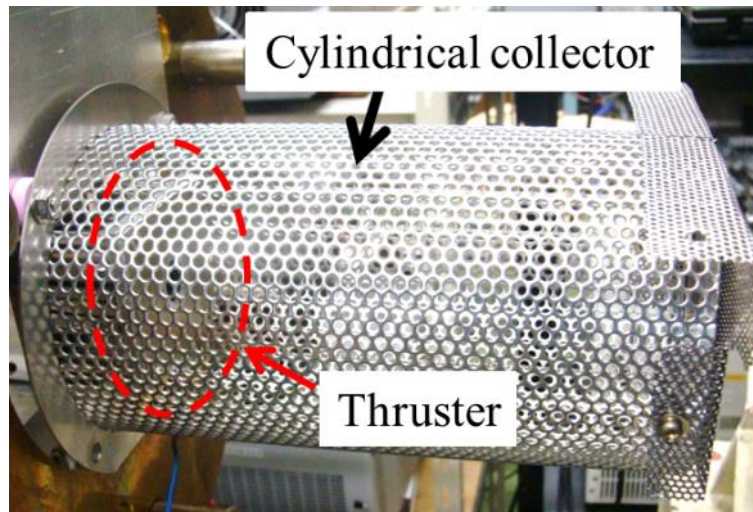


Fig. 3-15 Photo of the cylindrical collector

3.6 Thrust measurement

3.6.1 Hanging Pendulum Thrust Stand³⁴⁾

Thrust stand was used to measure the thrust directly. The thrust stand is divided to three types; hanging pendulum type, inverted pendulum type and torsional pendulum type. Hanging pendulum type can operate stably and easily. Inverted pendulum type can realize the high resolution, but the operation is unstably. Torsional pendulum type can realize high resolution, but the size of the stand is large. In this study, hanging pendulum type is adopted for simplicity. Fig. 3-16 shows the thrust stand used in this study. In this thrust stand, thruster is installed at the bottom of the pendulum, and the counter weight is installed in the top of the pendulum. Displacement is measured by the LED displacement sensor (Z4D-F04A, made by OMRON) and the displacement is calibrated by using weight. Eddy current damper is installed in the side of the bottom. Damping system is important to minimize a noise and reduce the time required to reach a stable position of the pendulum.³⁵⁾

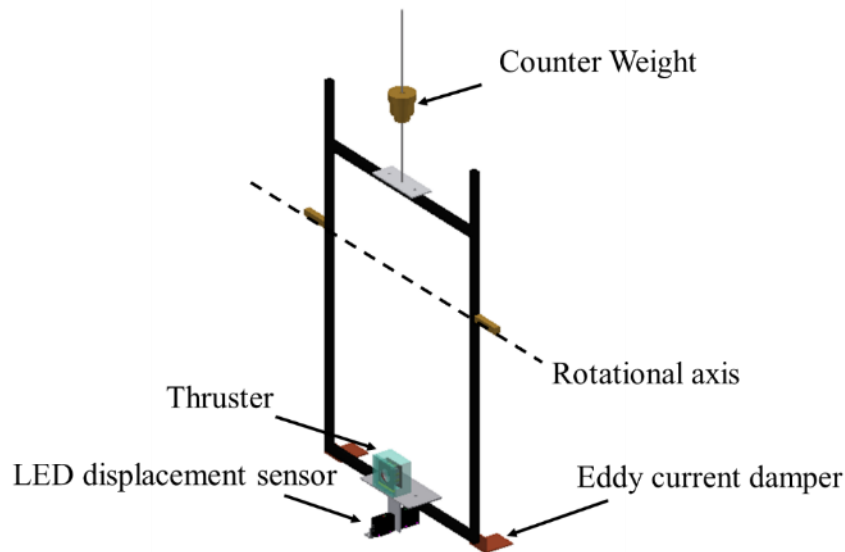


Fig. 3-16 Schematics of the thrust stand

3.6.2 Aluminum Target Thrust Stand

Thrust was also measured by using aluminum target. Figure 3-17 shows the Schematics of the thrust measurement by using aluminum target. Aluminum target is hung in front of the thruster. The distance of the thruster and aluminum target is 3 mm. Aluminum target is displaced by receiving the ion beam. The displacement is calibrated by using weight. The

number of weights pull the target is changed by taking up the thread using vacuum rotational feedthrough.

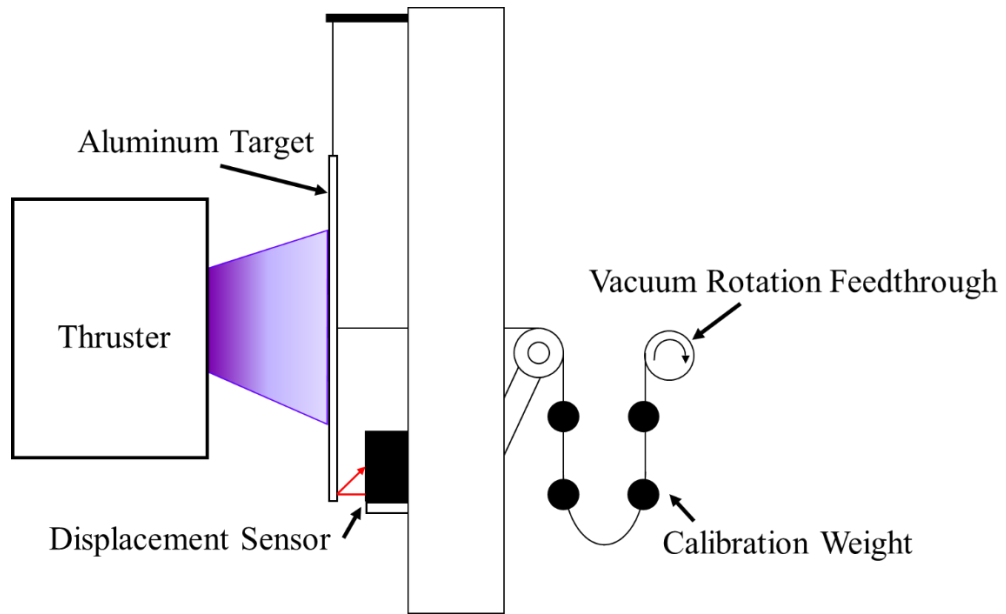


Fig.3-17 Schematics of the thrust measurement by using aluminum target

Chapter 4

Experimental Result and Discussion

4.1 Ion Energy Measurement

Ion beam was measured by RPA to confirm the acceleration of ion. The length of the discharge chamber is 33 mm and the number of magnets is 14. The diameter of the orifice is 12 mm. The mass flow rate is 82 $\mu\text{g}/\text{sec}$. In this experiment, thruster is connected to GND. This experiment is conducted in the large vacuum chamber in Kyusyu University. Fig. 4-1 shows the measured IEDF. The average ion energy was 13.7 eV, 18.4 eV and 19.3 eV for incident power of 10 W, 20 W and 32 W, respectively. The average ion energy increased with the increasing of the incident power. This is because the incident power per unit mass increase and electron temperature increase. As a result, the plasma potential of the discharge chamber increases and ion velocity increase. The acceleration was confirmed. The IEDF is not symmetric and is biased to the low energy side. This is caused by charge exchange collisions before the ion reaches the RPA from the thruster. Therefore, the average ion energy is underestimated.

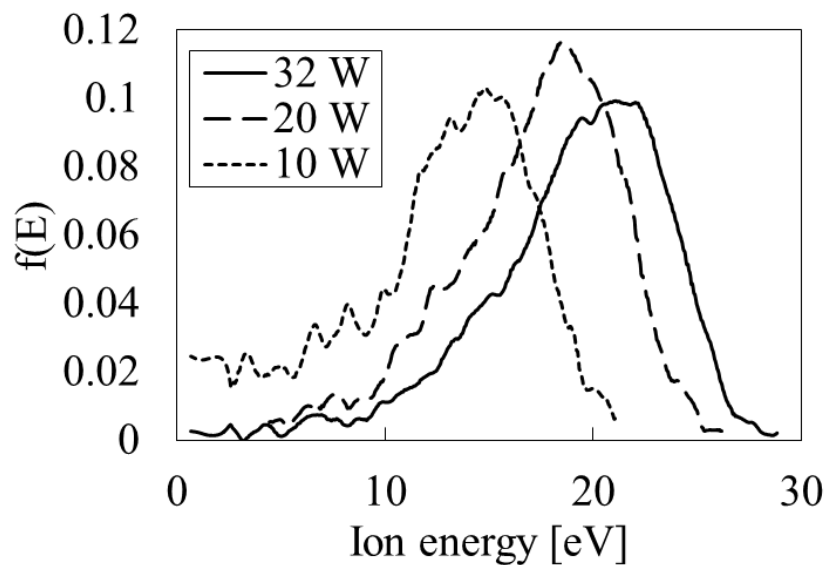


Fig. 4-1 Ion energy distribution function for several incident power

4.2 Plasma Diagnostics by Langmuir Probe

The plasma diagnostics is conducted by Langmuir probe. The length of the discharge chamber is 33 mm and the number of magnets is 14. The diameter of the orifice is 12 mm. The mass flow rate is 82 $\mu\text{g}/\text{sec}$. In this experiment, thruster is connected to GND. The Langmuir probe is installed in the linear actuator and inserted to the thruster from the downstream on the center axis of the thruster as shown in Fig. 4-2. Plasma potential is the discharge chamber at the deepest point in the discharge chamber was 19.0 V, 23.2 V and 25.4 V for incident power of 10 W, 20 W and 32 W, respectively. The plasma potential increase with the increasing of the incident power. This result is consistent with the IEDF measured by RPA. The potential difference was gentle than expected. The electron density and electron temperature in the discharge chamber was $7 \times 10^{17} \sim 2 \times 10^{18} \text{ m}^{-3}$ and 3~5 eV. There is some consideration in the Langmuir probe measurement. Firstly, electron density may be overestimated by the sheath effect. The surface area of the probe become big virtually and the electron current increase. Secondly, the electron saturation current decrease, so the potential may be underestimated and the electron temperature may be overestimated.

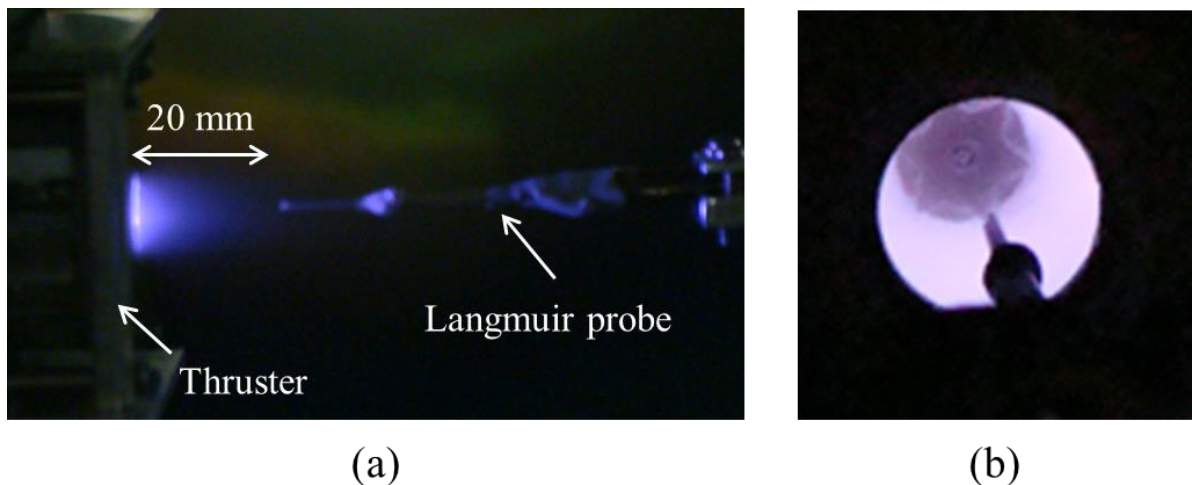
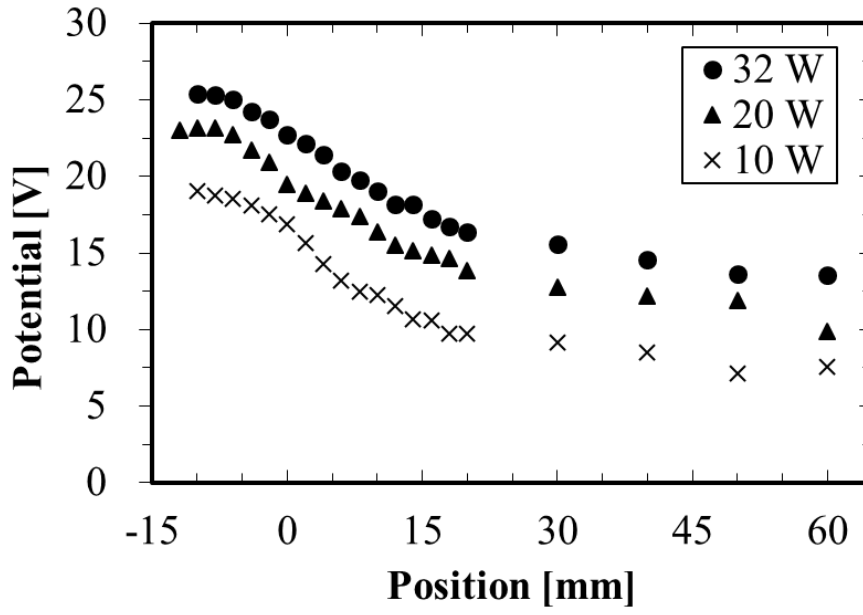
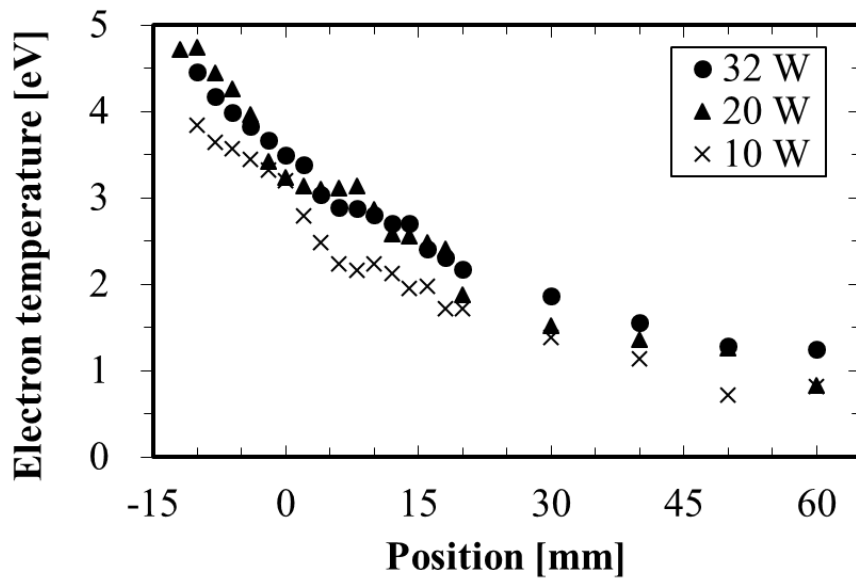


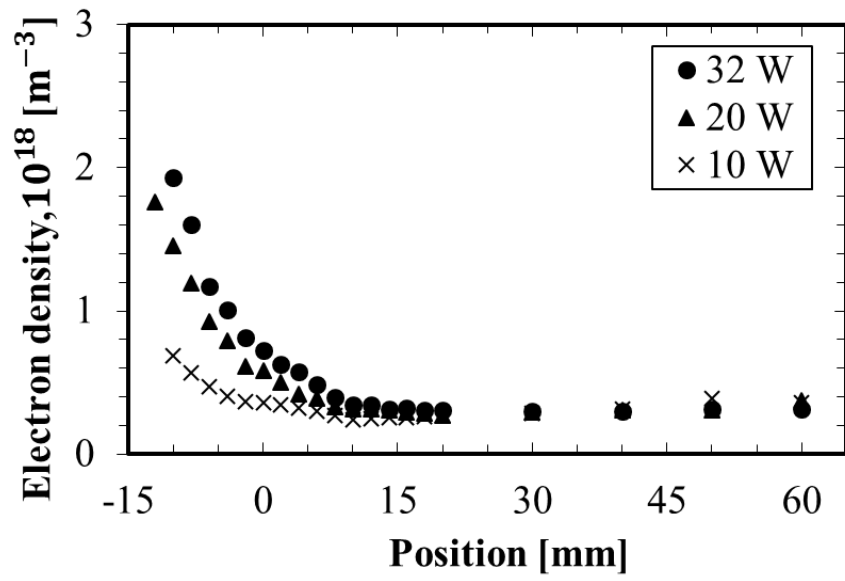
Fig. 4-2 Photo of the Langmuir probe measurement



(a)



(b)



(c)

Fig.4-3 Results of probe measurement, (a) Distribution of the potential, (b) Distribution of the electron density,(c) Distribution of the electron temperature.

4.3 Space Potential Measurement by Emissive Probe

Up to this point, ion acceleration and generation of the potential difference was confirmed with the thruster connected to GND. However, in practical operation, the thruster is floated electricity. Therefore, we measured the space potential distribution is measured by using emissive probe with the thruster floated electricity. In addition, the effect of the back ground plasma was investigated, because there is the weak plasma in the super low altitude. The length of the discharge chamber is 12 mm and the number of magnets is 6. The diameter of the orifice is 10 mm. This experiment is conducted in Space Science Chamber at the Institute of Space and Astronautical Science (ISAS) of Japan Aerospace Exploration Agency. In this experiment, the aluminum plate was connected to the thruster to keep the thruster potential equal to the space potential. The size of the plate is 27 cm × 42 cm. The plate is located in the side of the thruster as shown in Fig. 4-4.

Figure 4-5 shows the photo of the emissive probe measurement. Figure 4-6 shows the space potential distribution measured by emissive probe with the back ground plasma. The mass flow rate is 82 μg/s. The probe current is 10.55 A. As shown in this figure, the space potential inside the discharge chamber is 7.65 V, 7.75 V and 8.59 V at incident power of 10 W, 20 W and 30 W, respectively. These potentials are lower than expected, but the true potentials may be $1.5\sim 2T_e$ higher than the measured potentials by space charge effects.³⁶⁾ T_e is the electron temperature of the plasma around the emissive probe. The space potential in the discharge chamber increases with the increasing of the incident power. This is because the incident power per unit mass increase and the electron temperature increase. As a result, the space potential increases. This space potential inside the discharge chamber is about 10 V lower than the potential measured by the Langmuir probe. This difference seemed to be caused by the effect of the boundary condition of the vacuum chamber. In fact, the potential distribution measured by Langmuir probe is almost flat outside the discharge chamber. This means that IEDF measured by the RPA was overestimated about 10 eV which is correspond with the space potential at the point of the RPA installation. Therefore, the true potential difference generated by this thruster seemed to be about 10 V as shown in Fig. 4-6.

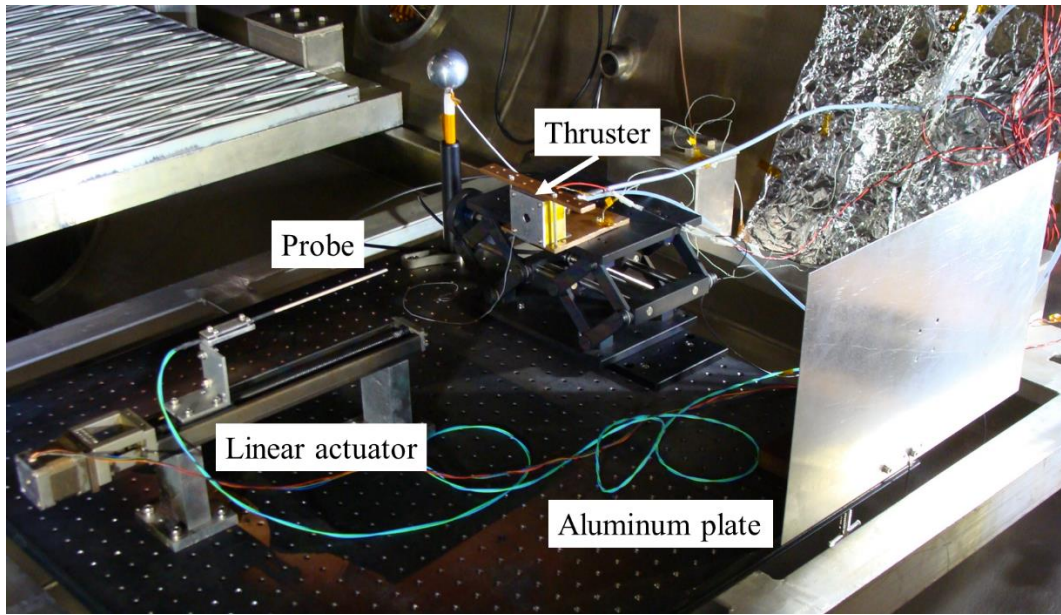
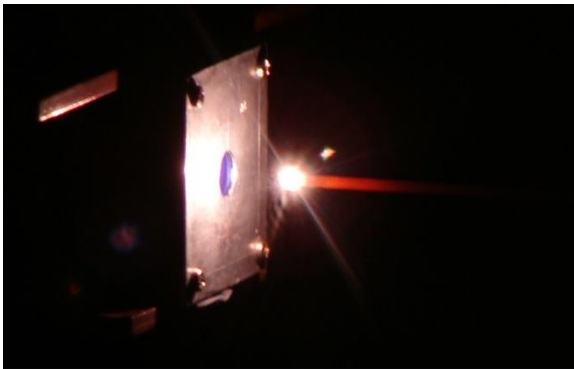
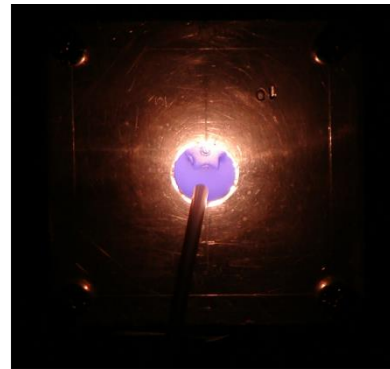


Fig. 4-4 Setup of the tether



(a)



(b)

Fig. 4-5 photo of the emissive probe measurement

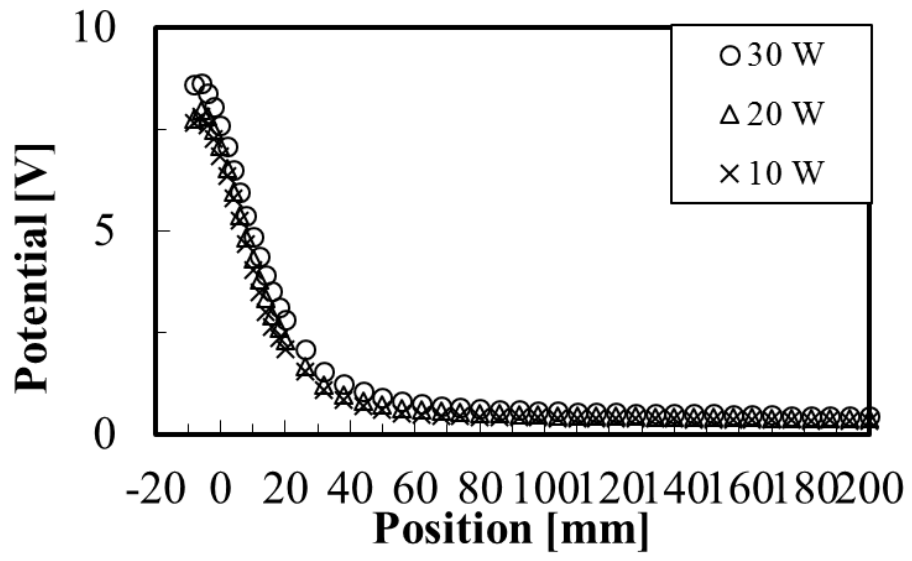


Fig. 4-6 Space potential distribution for several incident power

4.4 Thrust Performance Estimation

Up to the above section, the ion acceleration mechanism was investigated and the ion acceleration and the generation of the potential difference is confirmed. Next, we estimated the thrust performance. Thrust performance is estimated using ion beam current and ion velocity as shown in Eq. 2-3. Ion velocity is calculated from the potential difference measured by emissive probe. Ion beam current was measured by cylindrical collector to collect the scattered ion by charge exchange collision. The length of the discharge chamber is 12 mm and the number of magnets is 9. The diameter of the orifice is 12 mm. Thruster is connected to the GND. The mass flow rate is 82 $\mu\text{g}/\text{sec}$. This experiment was conducted in the small vacuum chamber in Kyushu University. Figure 4-7 shows the photo of the ion beam measurement. Figure 4-8 shows the ion beam current measured by cylindrical collector and plate collector. The ion beam current is 13.5 mA, 32.3 mA and 51.1 mA at the incident power of 10 W, 20W and 32 W. As shown in this Figure, the ion beam current measured by cylindrical collector is about twice of the ion beam current measured by the plate collector. This shows that about 50% of the exhausted ions were scattered by charge exchange collision. Considering the ions escape through the aperture of a perforated texture of the cylindrical collector, the measured ion beam current should be compensated. The coefficient of compensation is 1.91, which is the ratio between collector area and aperture area and it is determined by the assumption that the rate which ions escape is equal to the aperture ratio. This is because the Debye length is very small compared with the diameter of apertures. The Debye length estimated to be 50 μm outside of the thruster from past probe measurement and a diameter of apertures on the collector is 3 mm. This Debye length is estimated from the electron density ($1.0 \times 10^{16} \sim 4.0 \times 10^{16} \text{ m}^{-3}$) in the downstream obtained by ion saturation current. This estimation is supported by the additional experiment; the plate collector and perforated plate set in the sides of the thruster and ion beam current was measured. As a result, the ion beam current measured by the plate collector is approximately the twice the one of the perforated plate. The base of the cylindrical collector doesn't have aperture, so the coefficient of compensation doesn't correspond with the result. Table 4-1 shows the compensated ion beam current and estimated performance. Estimated thrust is 61 μN at the incident power of 10 W. This is under 1/10 of the objective thrust. However, the performance may be overestimated due to the effects of the confinement of neutral particles and possible uncertainties in the method

of the compensation.

For confirmation of the validity of this performance estimation, ion beam current was estimated by another method. Ion beam current was calculated by following equation.

$$V_o = \left(\frac{kT_e}{m_i} \right)^{\frac{1}{2}} \quad (4-1)$$

$$I_{in} = en_i V_o S \exp(-1/2) \quad (4-2)$$

Eq. (4-1) is the Bohm velocity. From this equation, the ion velocity at the sheath edge is obtained. Using this ion velocity, ion current in the discharge chamber is calculated from Eq. (4-2). In this equation, e , n_i and S are elemental charge, ion density and area. Ion density is assumed to be equal to electron density. S is the orifice diameter for simplicity. $\exp(-1/2)$ is used to calculate the density at the sheath edge from the density in discharge chamber. Table. 4-2 shows the results of the estimation. Comparing the compensated ion beam current shown in Table. 4-1 and estimated ion beam current shown in Table. 4-3, the difference is only 5% at incident power of 10 W. However, the difference is 20% and 50% at incident power of 20 W and 32 W. Even after taking into consideration the uncertainty of the Langmuir probe measurement, this difference is large. Therefore, direct thrust measurement is needed.

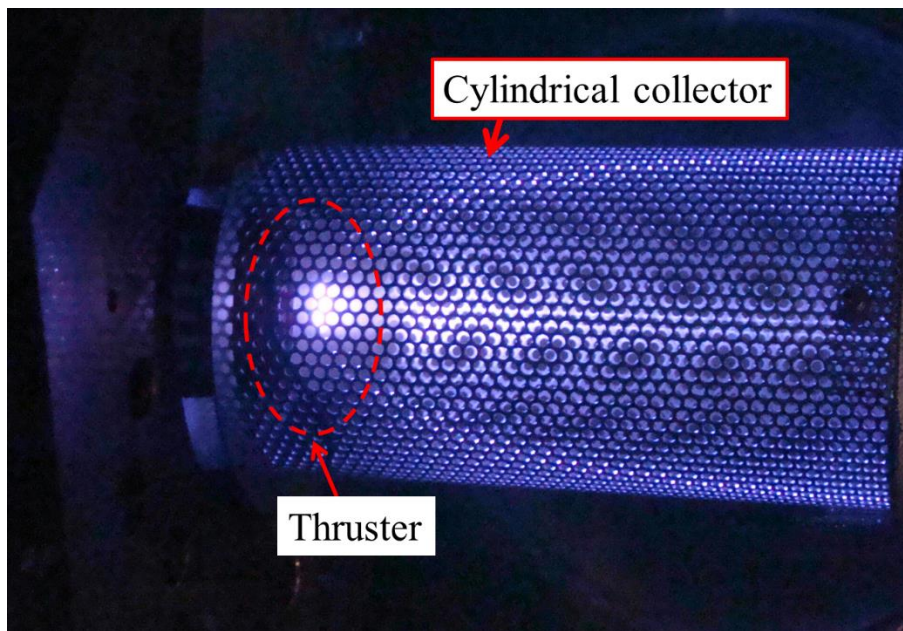


Fig. 4-7 Photo of the ion beam measurement

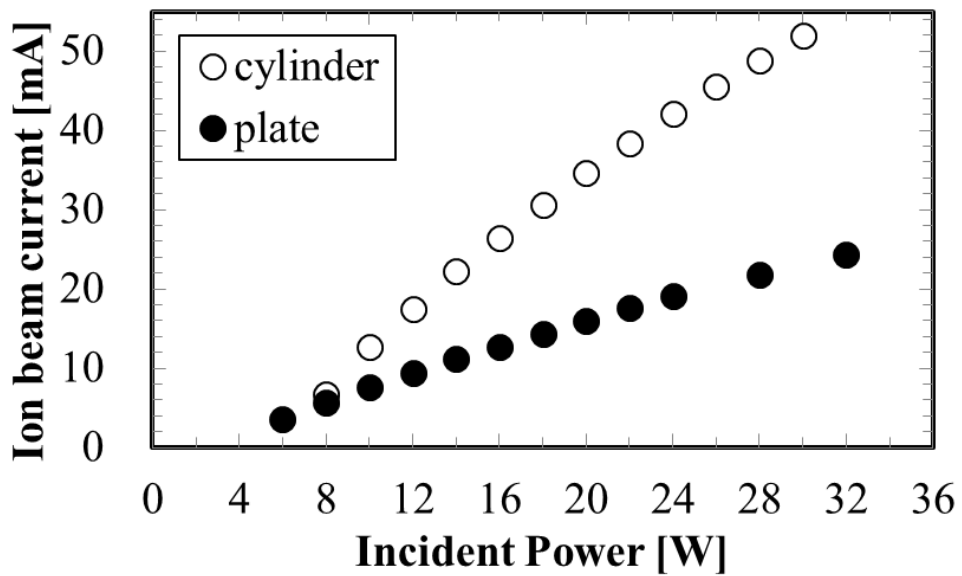


Fig. 4-8 Comparison of the ion beam measurement for cylindrical collector and plate collector

Table. 4-1 Estimated performance

Incident power	10 W	20 W	32 W
Ion beam current	24.2 mA	66.0 mA	105 mA
Thrust	61 μN	167 μN	280 μN
Specific impulse	75 sec	206 sec	345 sec
Propellant utilization	12%	33%	53%

Table. 4-2 Ion beam current in the discharge chamber

Incident power	10 W	20 W	32 W
Potential current	23 mA	54 mA	69 mA

4.5 Thrust Measurement

4.5.1 Measurement by Hanging Pendulum Thrust Stand

Thrust was measured by the pendulum thrust stand. This experiment was conducted in Space Science Chamber at the Institute of Space and Astronautical Science (ISAS) of Japan Aerospace Exploration Agency. At first, the displacement was calibrated by using weight. Before the experiment, the effect of the damper material to the attenuation of the oscillation was investigated. This investigation was conducted in the air. Fig. 4-9 shows the attenuation of the oscillation for several damper materials. As shown in this figure, the attenuation time is minimum when the damper material is copper. This seemed to be due to the low resistance of the copper. The M 2.6 washer was used as the calibration weight. However, the displacement for the weight is not constant. Fig.4-10 show the calibrated relation between the thrust and the voltage change of the displacement sensor. As shown in this figure, the dispersion was large. The obtained calibration coefficient is $0.864 \text{ V}/\mu\text{N} \pm 0.321 \text{ V}/\mu\text{N}$. The length of the discharge chamber is 12 mm and the number of magnets is 6. The diameter of the orifice is 10 mm. Thruster is floated electricity. The mass flow rate is $82 \mu\text{g}/\text{sec}$. Fig. 4-12 show the measured data when the microwave stopped. The incident power was 20 W. From this displacement, the thrust is estimated to be $54 \mu\text{N} \pm 20 \mu\text{N}$. However, this displacement might be not due to the thrust. Fig. 4-13 shows the measured displacement without plasma. As shown in this figure, the displacement is as much as the displacement with plasma vanishment. This seemed to be due to the elasticity changing of the microwave cable on account of the heating. Therefore, the reliability of the thrust estimated by this experiment is low.

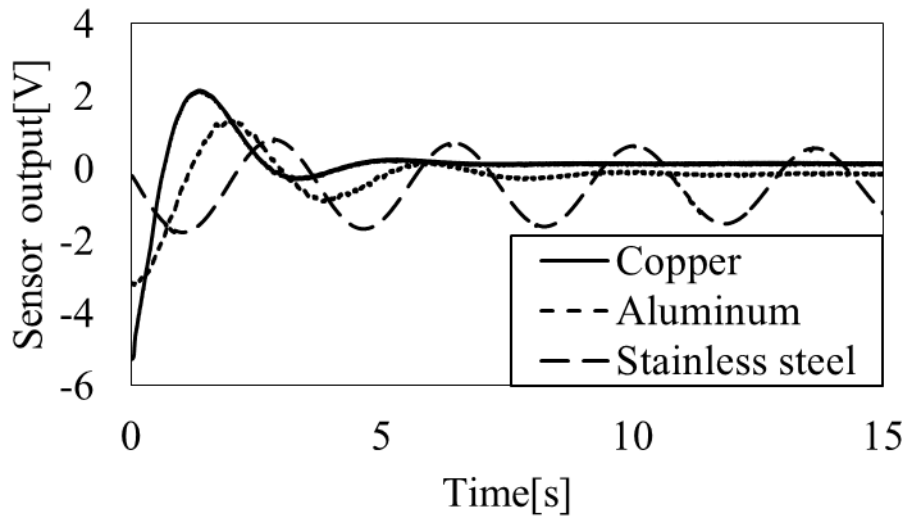


Fig. 4-9 The attenuation of the oscillation for several damper materials

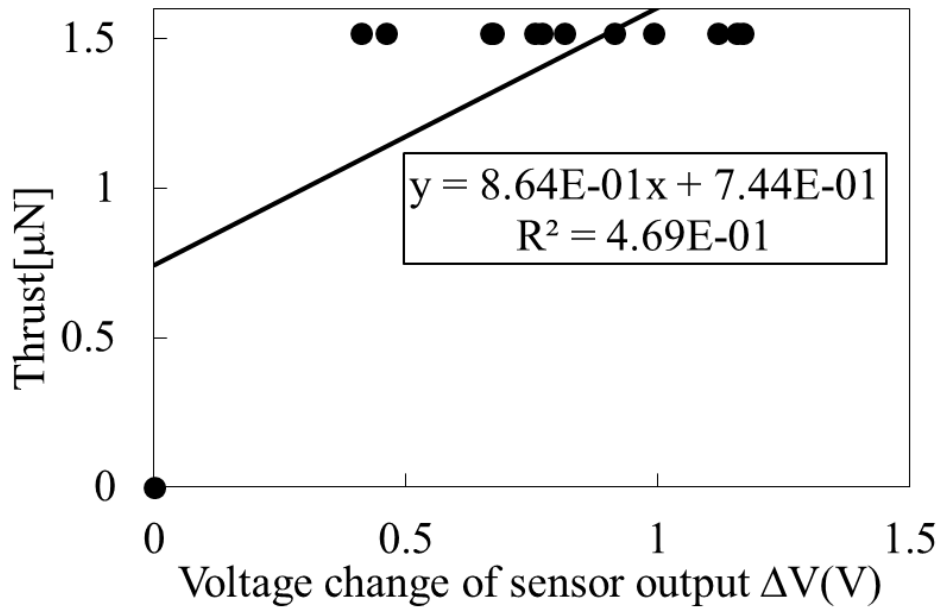


Fig. 4-10 Calibration result

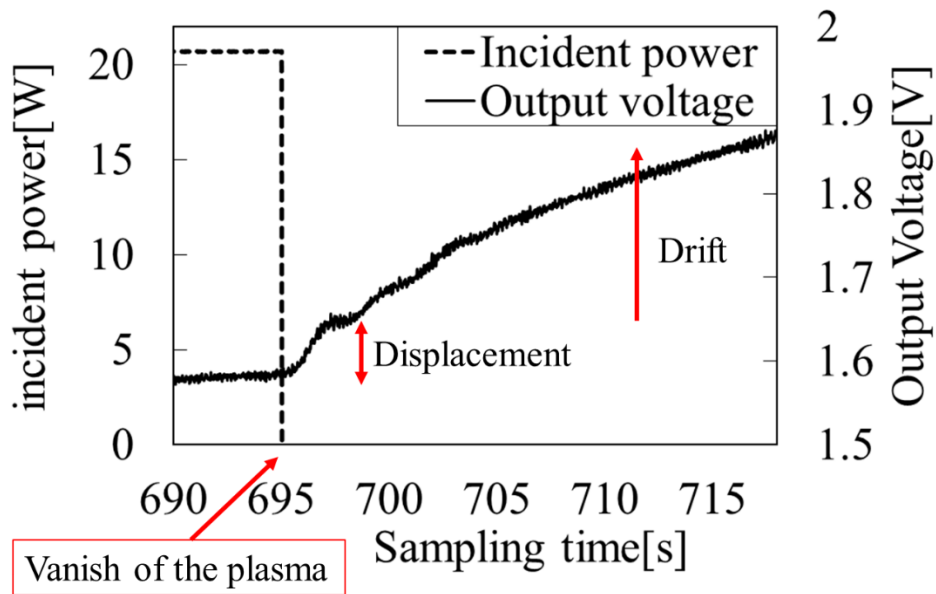


Fig. 4-11 Measured displacement

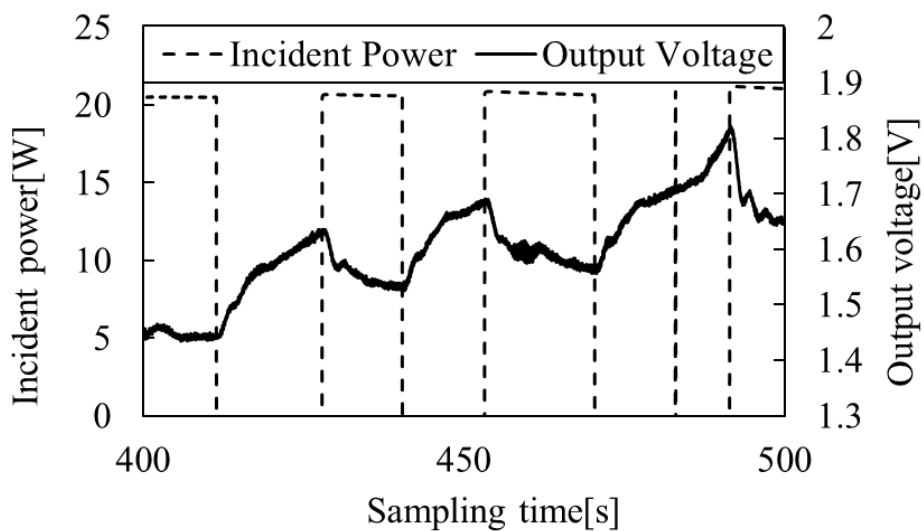


Fig. 4-12 Measured displacement without plasma

4.5.2 Measurement by Aluminum Target Thrust Stand

Thrust is also measured by using the aluminum target thrust stand. This experiment was conducted in the small vacuum chamber in Kyushu University. The diameter of the orifice is 10 mm and the number of magnets is 6. Thruster is floated electricity. The mass flow rate is 82 $\mu\text{g}/\text{sec}$. Fig. 4-13 shows the Photo of the thrust measurement by the aluminum target. The distance between the thruster and the target is 30 mm. The displacement was calibrated by the weight. However, displacement was not measured when the plasma

vanished with the calibration weight connected. This is because the friction force between the thread and the pulley. Therefore, the thrust was measured with the thread cut. The displacement was measured when the plasma was ignited and vanished. This means the thrust was generated by the thruster. The displacement increase with the increasing of the incident power and it is consistent with space potential and the IEDF showed in the above sections. However, the calibration coefficient became invalid because the mobility of the target changed by cutting the thread. Therefore, the thrust was estimated by the ideal relationship between the displacement and thrust. Fig. 4-14 shows the estimated thrust. Thrust was measured with the thruster connected the GND or floated. Thrust was 3.4 μN , 6.7 μN and 8.7 μN for incident power of 10 W, 20 W and 30 W, respectively. As shown in this figure, the difference of the thrust for two electrical state of the thruster is very small at incident power of 10 W and 20 W. Even when the incident power is 30 W, the difference is about 10%. Therefore, it seemed that the electrical state of the thruster doesn't affect to the thrust drastically. In this figure, the thrust doesn't include the contribution of the raw gas. This estimated thrust is much lower than expected. Therefore, we compared the thrust generated by the plasma and raw gas. The Figure. 4-15 shows the thrust measured when the diameter of the orifice is 12 mm and the number of magnets is 9. Thruster was connected to GND. The thrust was 8.6 μN , 17 μN and 22 μN at incident power of 10 W, 20 W and 30 W, respectively. Those thrust don't include the thrust of the law gas. As shown in this figure, the thrust generated by the plasma is almost same as the thrust of the law gas at incident power of 10 W. Even at incident power of 30 W, the thrust is only three times of the thrust of the low gas. These thrust are only 1/10 of the objective thrust. However, those thrust are 1/6~1/10 of the estimated thrust shown in section 4.4. There is some reason of this disagreement: error of the gas calibration, changing of the potential difference by aluminum target and overestimate of the ion beam current. In this experimental, calibration was conducted by using gas. However, the reaction of the gas and ion is different. All gas is reflected by target though some ion attach the target. Therefore, the thrust was underestimated by difference of the momentum transfer. The potential difference might be under 10 V by the effect of the aluminum target. As shown in section 4.2 and 4.3, the potential distribution was affected by boundary condition, especially the distance of the thruster and the aluminum target is close and it is 30 mm. Even there is no effect for the potential difference, the potential doesn't drop enough at the point of the aluminum target as shown in Fig. 4.6. The ion beam was overestimated as shown in section 4.4. Taking into

these error, it seemed that the practical thrust is between the estimated thrust from ion beam current and the measured thrust by aluminum target.

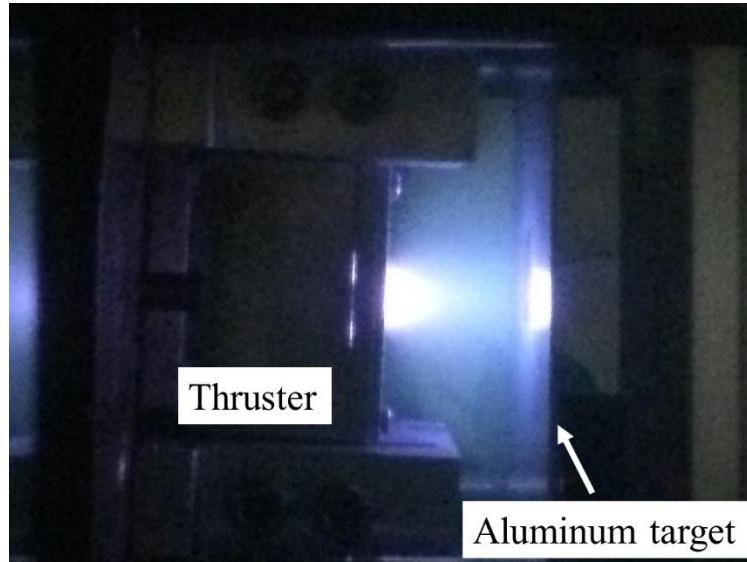


Fig. 4-13 Photo of the thrust measurement by the aluminum target

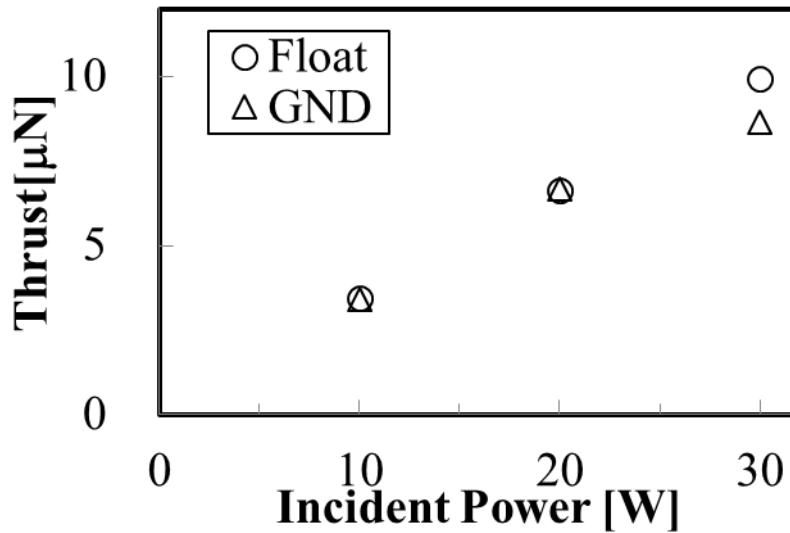


Fig. 4-14 Dependence of the thrust in the electrical state of the thruster

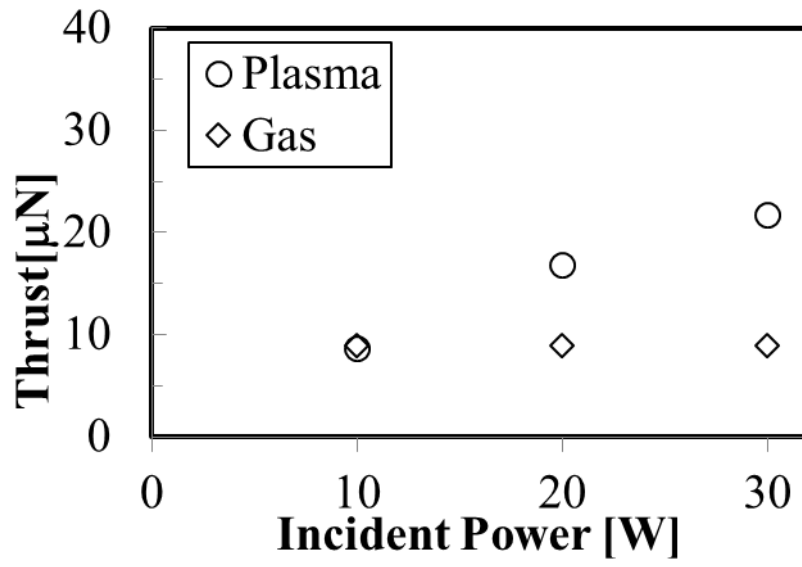


Fig. 4-15 Comparison of the thrust between the plasma and law gas.

Chapter 5

Summary

We investigated the ion acceleration mechanism of the miniature microwave discharge thruster and estimated the thrust performance. The results is showed as following.

1. Ion acceleration was confirmed by using RPA.
2. The generation of the potential difference was confirmed even in the back ground plasma. The potential difference is about 10 V and it is the half of the expectation.
3. Thrust performance was estimated from the ion beam measured by using cylindrical collector. The estimated performance was 61 μN at incident power of 10 W.
4. It was tried that the thrust measurement by pendulum thrust stand. However, it failed by the elasticity changing of the microwave cable.
5. The thrust was also measured by the aluminum target and the generation of the thrust was confirmed. The thrust was 8.6 μN .

In this study, the ion acceleration and the generation of the potential difference was confirmed. However, the mechanism of the potential difference generation remains unclear. The investigation about these mechanism is important for improving of the thrust performance. In future, the simulation code should be established for elucidation of the mechanism. After that, the thrust should be measured directly by more reliable method for accurate evaluation of the thrust performance.

List of Reference

- [1] Kaneoka, M.: A summary and task of Nano/Micro satellites, Proceedings of 58th Space Sciences and Technology Conference, Nov. 2014 (in Japanese).
- [2] Yamazaki M.: Mission of Piggy –back Satellite SPROUT Launched with ALOS –2, The Institute of Electronics, Information and Communication Engineers, 112 (2012), pp.77-81 (in Japanese).
- [3] Yoshihiro, T., Hanada, T., Van der Ha, J.: QSAT: A Low-Cost Design for 50kg Class Piggyback Satellite, Proceedings of 26th International Symposium on Space Technology and Science, Jun. 2008.
- [4] Matunaga, S.: Dream and reality of Nanosatellites, International Journal of Microgravity Science Application, 30 (2013), pp. 136-142 (in Japanese).
- [5] Sastrokusumo, U., Lumanto, R.: LAPAN A2 Micro Satellite and the Need for Rapid Emergency Communication, Proceedings of 29th International Symposium on Space Technology and Science, Jun.2013.
- [6] Kawano, I., Ymamoto, T., Mitani S.: Application of formation flying technology to frontier space missions, The Institute of Electronics, Information and Communication Engineers, 109 (2009), pp.127-132 (in Japanese).
- [7] Maeda, K.: Present and future of near earth satellite mission: Applications to Observation and Communication system of small satellites, The Institute of Electronics, Information and Communication Engineers,112 (2012), pp.173-180.
- [8] Tsuruda, Y., Nakasuka S., Matsui, M., Mase, I.: Reasonably Reliable System Design and Operation for Twin Satellite: Hodoyoshi-3 & 4, Proceedings of 58th Space Sciences and Technology Conference, Nov.2014 (in Japanese).
- [9] Koizumi, H., Kasagi, Y., Inagaki, T., Kawahara, H, Yaginuma, K., Asakawa, J., Komurasaki, K.: Development of small propulsion system for nano-satellites and its challenges for the future, Proceedings of 58th Space Sciences and Technology Conference, Nov. 2014 (in Japanese).
- [10] Konoue, K, Imamura, S, Satoh Y, Kawasaki, H, Kohata, H.: Development Status of Super Low Altimde Test Satellite “SLATS”, The Institute of Electronics, Information and Communication Engineers, 111 (2011), pp.1-5 (in Japanese).
- [11] Xu, M., Zhou, N.: Image Positioning Accuracy Analysis for Super Low Altitude Remote Sensing Satellites, International Journal of Advanced Robotic Systems, Rijeka, Croatia, 9 (2012).
- [12] Fujita, K., Noda, A.: Rarefied Aerodynamics of a Super Low Altitude Test Satellite (SLATS), Proceedings of 41st Fluid Dynamics Conference / Aerospace Numerical Simulation Symposium, Jun. 2009.

- [13] Arakawa, Y., Kuninaka, H., Nakayama, Y., Nishiyama, K.: Ion Engine for Power Flight in Space, Corona Publishing, Tokyo(2006), pp.125.
- [14] Koizumi, H., Kuninaka, H.: System Performance of a Microwave Discharge Miniature Ion thruster, Journal. Jpn. Soc. Aeronaut. Space Sci, 60(2012), pp.128-134 (in Japanese).
- [15] Kuriki, K., Arakawa, Y.: Introduction to Electric Propulsion, University of Tokyo Press, Tokyo (2003), pp.99.
- [16] Hoskins, W. A., Cassady, R. J., Morgan, O., Myers, M. R., Wilson, F., King, Q. D., deGrys, K.: 30 Years of Electric Propulsion Flight Experience at Aerojet Rocketdyne, Proceedings of the 33rd International Electric Propulsion Conference, Oct.2013.
- [17] Wallace, N., Jameson, P., Saunders, C., Fehringer, M., Edwards, E., Floberghagen, R.: The GOCE Ion Propulsion Assembly – Lessons Learnt from the First 22 Months of Flight Operation, Proceedings of the 32nd International Electric Propulsion Conference, Sep.2011.
- [18] Cannat, F., Jarrige, J., Lafleur, T., Elias, P.-Q., Packan, D.: Experimental geometry investigation of a coaxial ECR plasma thruster, Proceedings of the 34th International Electric Propulsion Conference, Jul.2015.
- [19] Sheehan, P.J., Collard, A.T, Ebersohn, H.F., Longmier, W.B.: Initial Operation of the CubeSat Ambipolar Thruster, Proceedings of the 34th International Electric Propulsion Conference, Jul.2015.
- [21] Hirano, K.: Development of $E \times B$ Probe for the Various Electric Propulsion, Master Thesis of Kyushu University, 2013.
- [22] Toyoda, Y., Ushio, K., Yamamoto, N., Nakashima, H.: Development of a Miniature Microwave Discharge Plasma Thruster, Journal of IAPS, 21 (2013), pp.103-108 (in Japanese).
- [23] Funaki, I., Kuninaka, H., Toki, K.: Plasma Characterization of a 10-cm Diameter Microwave Discharge Ion Thruster, Journal of Propulsion and Power, 20 (2004), pp. 718-726.
- [24] Miyoshi, M.: Development of a Ion Engine Using Argon, Master Thesis of Kyushu University, 2008
- [25] Kusuda, M.: Analysis of the extraction current and voltage in a microwave discharge neutralizer, Master Thesis of Kyushu University, 2014.
- [26] Kuninka, H.: Round-Trip Deep Space Maneuver of Microwave Discharge Ion Engines onboard HAYABUSA Explorer, Proceedings of the 32nd International Electric Propulsion Conference, Sep.2011.
- [27] Ushio, K.: Development of a Novel Miniature Thruster Using Microwave Discharge, Bachelor's Thesis, Department of Advanced Energy Engineering Science, Kyushu University, Fukuoka (2011) (in Japanese).

- [28] Francis, F.C.: INTRODUCTION TO PLASMA AND CONTROLLED FUSION, Plenum Press, New York (1984), pp.33.
- [29]Ushio, K.: Development of a Novel Miniature Thruster Using Microwave Discharge, Bachelor's Thesis, Department of Advanced Energy Engineering Science, Kyushu University, Fukuoka (2011) (in Japanese).
- [30]Toyoda, Y., Ushio, K., Yamamoto, N., Nakashima, H.: Development of a Miniature Microwave Discharge Plasma Thruster, Journal of IAPS, **21** (2013), pp.103-108 (in Japanese).
- [31]Teii, S.: Fundamental Engineering of Plasma Augmented Edition, UCHIDA ROKAKUHO PUBLISHING, Tokyo (1997), pp.125-219.
- [32]Reijen, B. V., Weis, S., Lazurenko, A., Haderspeck, J., Genovese, A., Holtmann, P.: High Precision Thrust Vector Determination through Full Hemispherical RPA Measurements assisted by Angular Mapping of Ion Energy Charge State Distribution, Proceedings of the 33rd International Electric Propulsion Conference, Oct.2013.
- [33]Toyoda, Y.: Development of a Miniature Microwave Discharge Thruster, Master Thesis of Kyushu University, 2014.
- [34]Polk, E.J, Pancotti, A., Haag, T., King, S., Walker, M.: Recommended Practices in Thrust Measurement, Proceedings of the 33rd International Electric Propulsion Conference, Oct.2013.
- [35]Koizumi, H., Kakami, A., Komurasaki, K., Arakawa, Y.: A Thrust Stand for Low-Power Electric Propulsion, Journal. Jpn. Soc. Aeronaut. Space Sci, **51**(2013), pp.270-275 (in Japanese).
- [36]Sheehan, P. J., Raitses, Y., Hershkowitz, N.: Accurately Determining the Plasma Potential Using Emissive Probes, Proceedings of the 33rd International Electric Propulsion Conference, Oct. 2013.

Acknowledgements

I would like to express the deepest appreciation to my supervisors; Emeritus Professor Hideki Nakashima, Associate Professor Naoji Yamamoto, and Assistant Professor Taichi Morita.

I would like to thank my labmates; Lee Hou-Yi, Naoya Saito, Koichi Ushio, Yu Okuda, Kohei Takase, Kazuhiko Nakano, Atsushi Yamaguchi, Kensuke Iijima, Tomohiro Ichimaru, Bunsuke Ueno, Yusuke Egawa, Masafumi Edamoto, Parsa Yousefian, Satoshi Miura, Yutarou Itadani, Masataka Iwamoto, Yutarou Kawahara, Hirotaka Fuchigami and graduates in my laboratory.

Some research results were obtained using Space Science Chamber is Space Plasma Laboratory of ISAS, JAXA.

Finally, I would like to express the deepest gratitude to my family for their kind support and help.